ISSN 0389-4010
UDC 621. 456. 2. 022. 5
536. 246

TECHNICAL REPORT OF NATIONAL AEROSPACE LABORATORY

TR-1062T

Hot Gas Side Heat Transfer Characteristics of LOX/H2 and LOX/HC Type Propellants

Akinaga KUMAKAWA, Masaki SASAKI, Kazuo SATO, Hiroshi TAMURA
Fumiei ONO, Hiroshi SAKAMOTO and Nobuyuki YATSUYANAGI

April 1990

NATIONAL AEROSPACE LABORATORY

CHŌFU, TOKYO, JAPAN

Hot Gas Side Heat Transfer Characteristics of LOX/H2 and LOX/HC Type Propellants*

Akinaga KUMAKAWA**, Masaki SASAKI**, Kazuo SATO**, Hiroshi TAMURA**,
Fumiei ONO**, Hiroshi SAKAMOTO** and Nobuyuki YATSUYANAGI**

ABSTRACT

Combustion tests were conducted using liquid oxygen (LOX)/gaseous hydrogen, LOX/gaseous methane and LOX/RJ-1J as propellants. Two water-cooled calorimetric combustors and two types of injectors, i.e., a coaxial and an impinging injector, were used. The maximum chamber pressure was 10 MPa and the heat flux reached 100 MW/m^2 in the maximum.

Heat flux values measured at the throat section were lower than those predicted by the simplified Bartz's equation. A modified Bartz's equation, which uses 0.023 as a coefficient (instead of 0.026 as in the original) and which takes into account the injector end effect as well as the film cooling effect, more accurately predicted the measured heat flux distribution of the coaxial type injector. With regard to LOX/RJ-1J propellants, an empirical correlation for the thermal resistance of the carbon layer deposited on the chamber wall was obtained. It was observed that the values of thermal resistance measured were a small percentage of the values found in previously published data.

概　　要

液酸 / ガス水素，液酸 / ガスメタンおよび液酸 /RJ-1J を用いた水冷却高圧燃焼試験を最大燃焼圧10MPa，最大熱流束100MW/m^2 の範囲で実施した。ここでは各推進剤における燃焼ガス側熱伝達特性について比較検討した。さらに液酸 /RJ-1J 系において壁面上に生じたカーボン層の熱抵抗について論じた。

実験により同軸噴流型エレメントを有する噴射器を使用した液酸 / ガス水素，及び液酸 / ガスメタンの場合の熱流束分布は，噴射器近傍からスロートに至る範囲では計算値とほぼ一致した。

また，噴流衝突型エレメントを有する噴射器を使用した液酸 /RJ-1J の場合の熱流束分布は計算値よりかなり低い値を示した。この原因として炭化水素系燃料に特有な，燃焼ガス中のカーボンが燃焼室壁に堆積したことによる熱抵抗の影響と推定された。この熱抵抗の値は，同一の燃焼ガス質量流束の下では従来のデータの数％であることがわかった。

Nomenclature

Cg	coefficient of simplified Bartz's equation
Dc	diameter of injector faceplate
G	mass flux of combustion gas
hg	hot gas side heat transfer coefficient
hg, ∞	hg far from injector faceplate
kc	thermal conductivity of the carbon deposition layer
N	number of coaxial element
O/F	mixture ratio
Pc	chamber pressure
q	heat flux
Mt	total propellant mass flow
TF, inj	fuel injection temperature
Tf	fuel injection temperature

* Received 13 February, 1990
** Kakuda Research Center

tc	thickness of the carbon deposition layer
ΔTsat	wall superheat
Tw	wall temperature
UR	injection velocity ratio
x	axial distance from nozzle throat
Xc	axial distance from injector
ηc*	C* efficiency
φinj	injector end effect
ε	film cooling efficiency

Subscript

cy	cylindrical
exp	experiemental
jout	coolant jacket outlet
NB	nucleation boiling
PB	preburner
ref	reference
th	nozzle throat

1. INTRODUCTION

Many studies on future booster rocket engines have recently appeard (Ref. 1–5). They are especially concerned with the Space Transportation Booster Engine (STBE) and the Space Transportation Main Engine (STME) for use in the Shuttle-2 (Ref. 1–3), as well as with the advanced HM-60 using LOX/methane (Ref. 4) and the advanced LE-7 (Ref. 5). Advanced rocket combustors are characterized by higher combustion chamber pressure and higher performance than previous combustors. Liquid hydrogen, liquid methane and heavy hydrocarbon of the RP-1 class are the most feasible fuels for these combustors.

The maximum heat fluxes of thrust chambers of typical liquid rocket engines are shown in Fig. 1. Hydrogen fueled rocket engines, such as the Space Shuttle Main Engine (SSME) and the LE-7, operate at combustion pressures of more than 14 MPa, and a combustion efficiency of about 99% can be achieved when these engines are employed in the staged combustion cycle. The maximum heat fluxes lie in the order of 100 MW/m^2.

The chamber pressures of previous hydrocarbon fueled engines were limited to 7.8 MPa as the case in the F-1 engine because of combustion instability and cooling problems. The maximum heat fluxes of the hydrocarbon fueled enignes are much lower than those of hydrogen fueled engines. The combustion efficiency of these hydrocarbon engines had to be about 94% in order to achieve stable combustion. Due to incomplete combustion and fuel film cooling systems requiring more than 10% of the fuel flow rate, the chamber walls of the combustors were coated with an insulation carbon soot layer as shown in Fig. 2. The insulation layer reduced heat input into the wall. It, therefore, enabled regenerative chamber cooling when using high density fuel, which easily causes coking under conditions of lower wall temperature.

In experiments with LOX/hydrocarbon propellants, Pavli (Ref. 6) has demonstrated the possibility of a high combustion efficiency level of 99 to 100% without

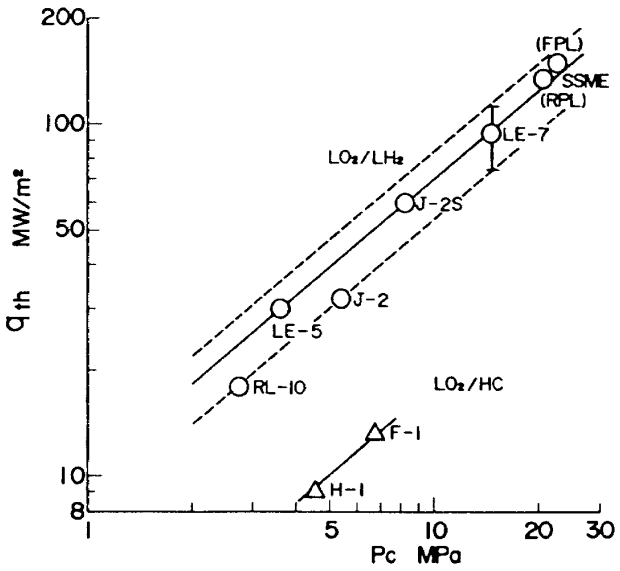

Fig. 1 Maxmium heat fluxes and chamber pressures of typical rocket engines

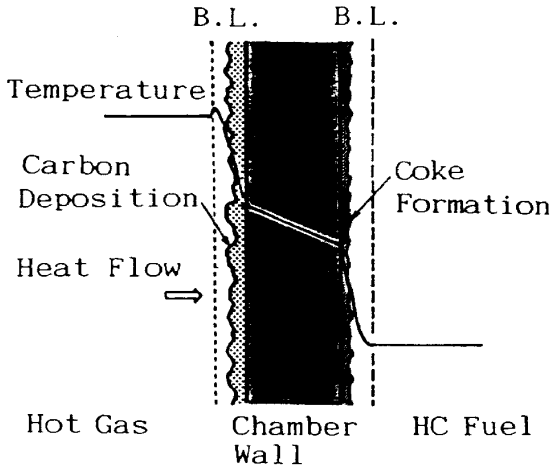

Fig. 2 Heat transfer aspect across the wall of hydrocarbon fuel thrust chamber

combustion instability. Thus high pressure LOX/hydrocarbon rocket engines with liquid hydrogen as a coolant have become feasible. However, there are contradictory existing data on the thermal resistance of the soot layer under high chamber pressure and in the presence of high combustion efficiency.

On the other hand, in order to achieve a desirable distribution of wall temperature and to determine a level of heat input to the coolant through the chamber wall which can drastically improve the performance of expander and gas generator cycle rocket engines, it is also necessary to accurately predict the hot gas side heat transfer coefficient under elevated chamber pressures. The phenomena which occur within the thrust chamber are extremely complicated. The heat transfer coefficient and hot gas temperature distributions within the thrust chamber are strongly affected by combustion parameters such as chamber pressure, mixture ratio and the combustion process (including the atomization of the liquid oxygen jet and/or the liquid fuel jet, its vaporization, as well as its mixing, combustion and the recirculation of combustion gas). Axial heat flux distribution also varies depending on the existence of film cooling and/or transpiration cooling in the injector. A carbon layer as an insulator may decrease the heat transfer to the wall in the case of hydrocarbon fuels. Strong combustion instability increases the heat transfer and may cause the wall of the chamber and the injector face plate to melt down.

The purpose of this study is to experimentally demonstrate the heat transfer characteristics of several propellants, LOX/hydrogen, LOX/methane and LOX/RJ-1J, at high chamber pressures, up to 10 MPa, and to investigate the effect of soot deposition on heat transfer in the case of LOX/hydrocarbon propellants.

2. APPARATUS

2.1 Injectors

Injectors with 18 coaxial elelments were employed in LOX/hydrogen and LOX/methane firing tests. The assemblies of these injectors are shown in Fig. 3. Twelve film cooling holes were drilled into the rigimesh faceplates of the injectors when necessary. Two injectors with FOF and FOOF impinging elements, as shown in Fig. 4, were employed in LOX/RJ-1J tests without film cooling. The geometric and operating characteristics of these injectors are shown in the references (Ref. 7–9). A water-cooled cavity ring was installed to prevent combustion instability in cases where it was necessary to use when LOX/methane and LOX/RJ-1J propellants were used.

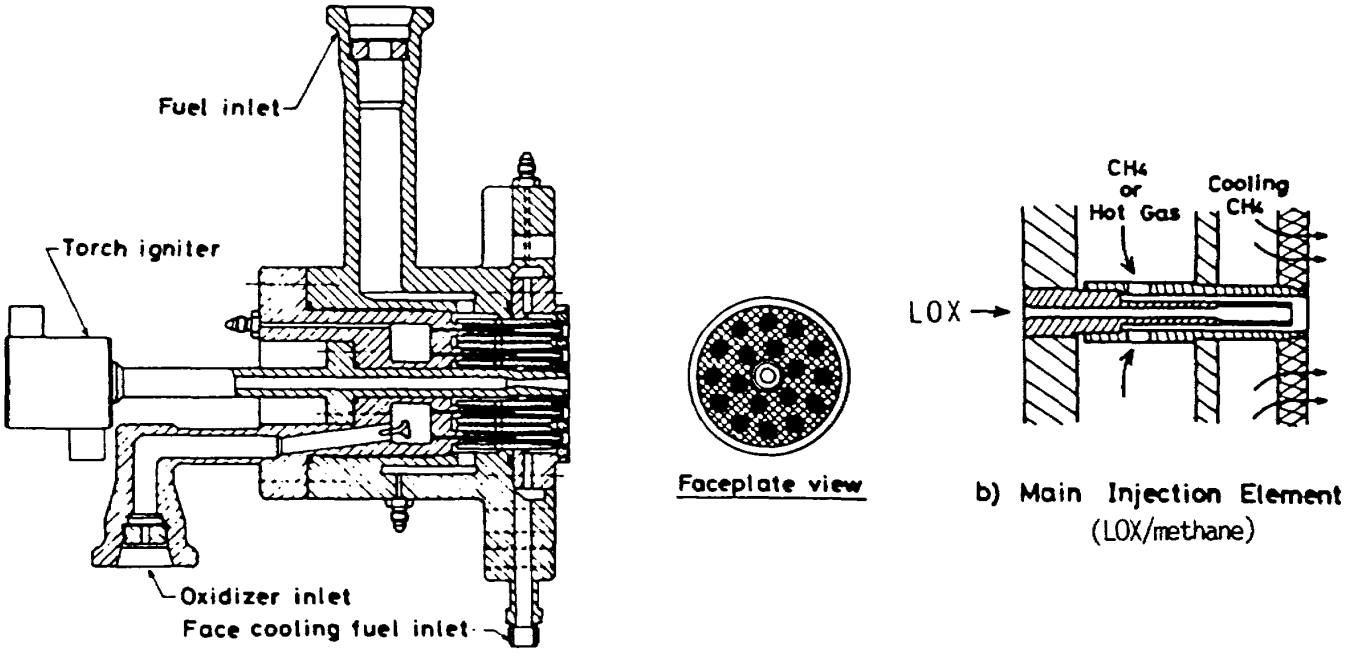

Fig. 3 Injector with 18 coaxial elements

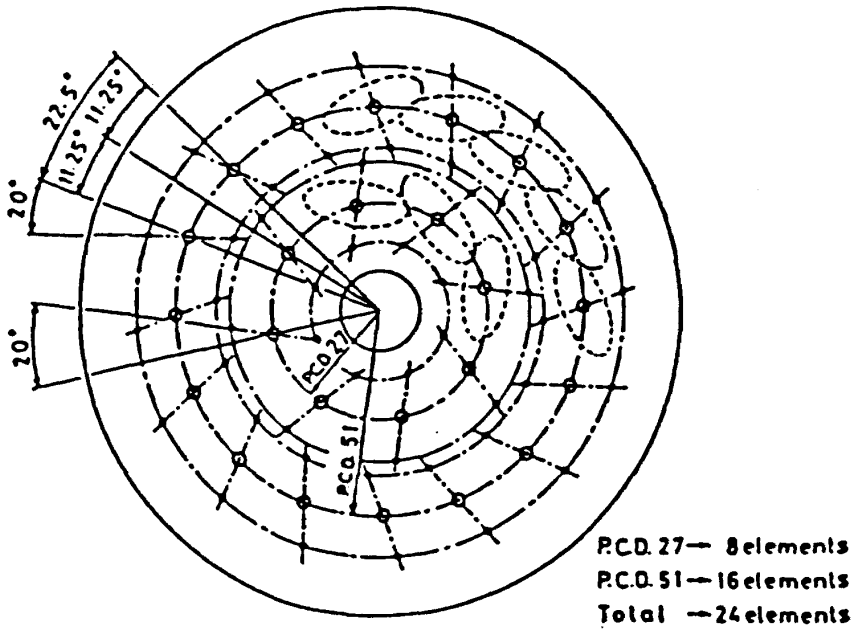

a) Pattern of injector elements

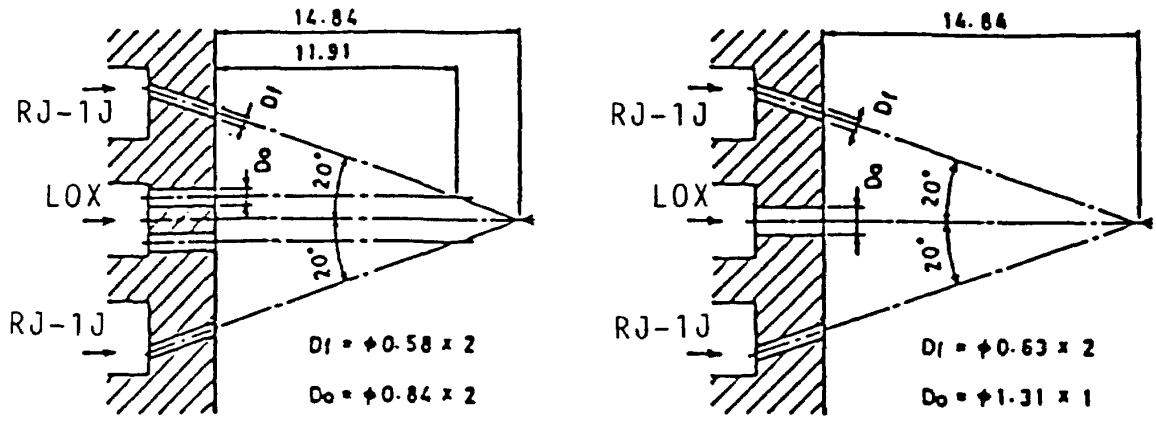

1) FOOF split triplet element

2) FOF triplet element

b) Injection elements

Fig. 4 Injector with FOF and FOOF impinging elements

2.2 Chambers

Two water-cooled calorimetric chambers were employed to measure the axial distribution of heat flux to the chamber wall. They consisted of 23 or 27 circumferential cooling channels, respectively, and had equal contours with the exception of the length of the cylindrical section. The 27-channel chamber is 50 mm longer than the 23-channel chamber. The 23-channel calorimetric chamber and the 27-channel chamber with a water cooled cavity ring are respectively shown in Fig. 5 and Fig. 6. The channels were machined into an OFHC (Oxygen Free High Conductivity) copper shell as shown in Fig. 7 and covered with stainless steel outer rings by means of electron beam welding as shown in Fig. 8. The cooling side of the channels had small triangular fins positioned at a 30-degree angle in order to enhance heat transfer coefficients on the coolant side. The boiling characteristics of the surface having fins at a 30-degree angle are shown in Fig. 9 in contrast with those of fins at a 60-degree angle. Both fins were machined along the

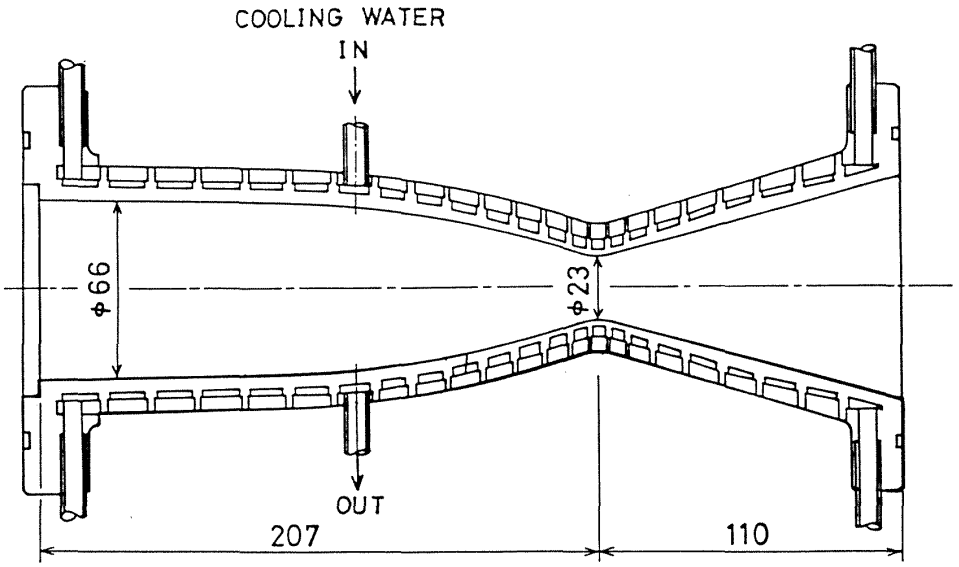

(a)

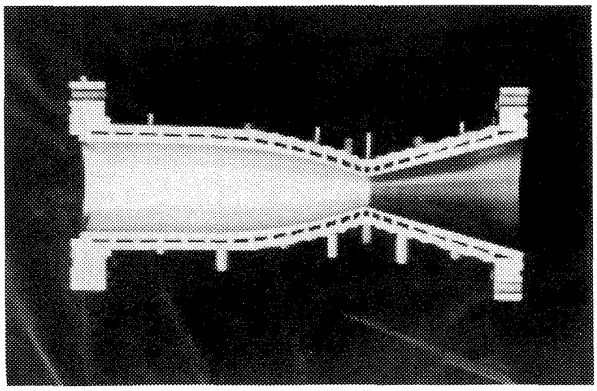

(b)

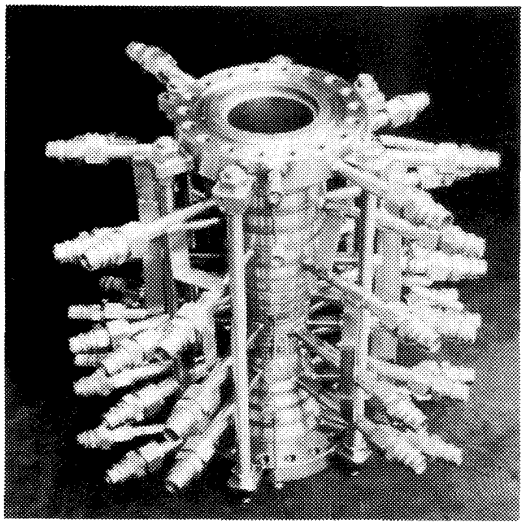

(c)

Fig. 5 23-channel water-cooled calorimetric chamber

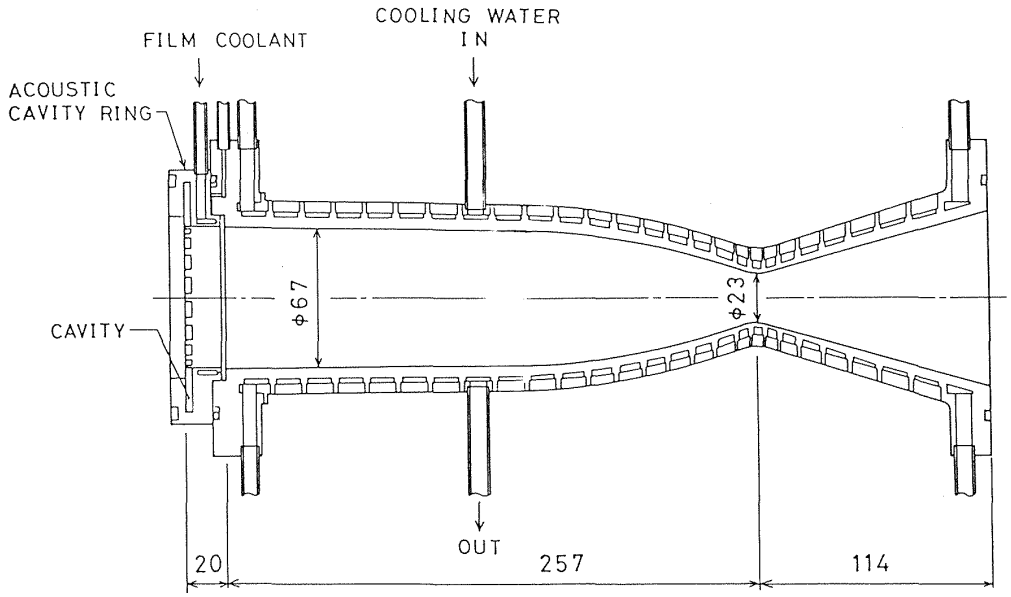

Fig. 6 27-channel water-cooled calorimetric chamber with a cavity ring

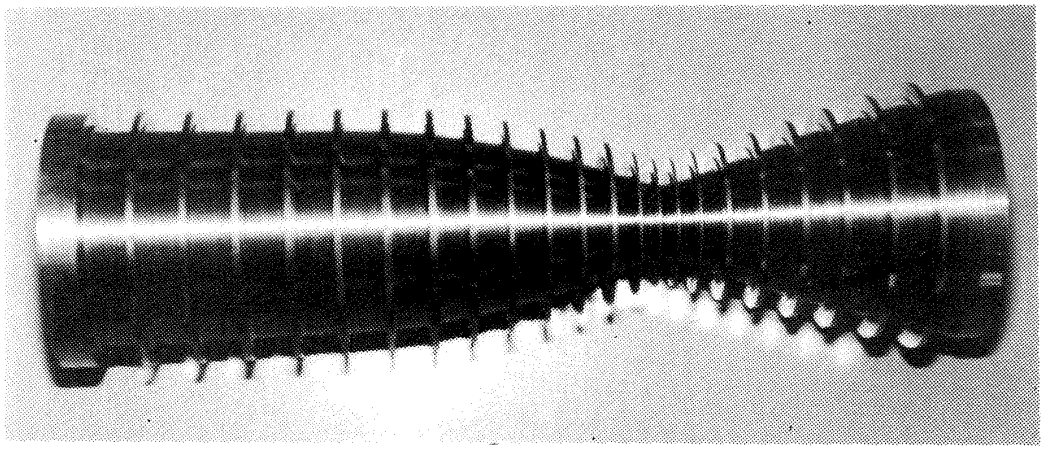

Fig. 7 Copper inner shell of water-cooled chamber

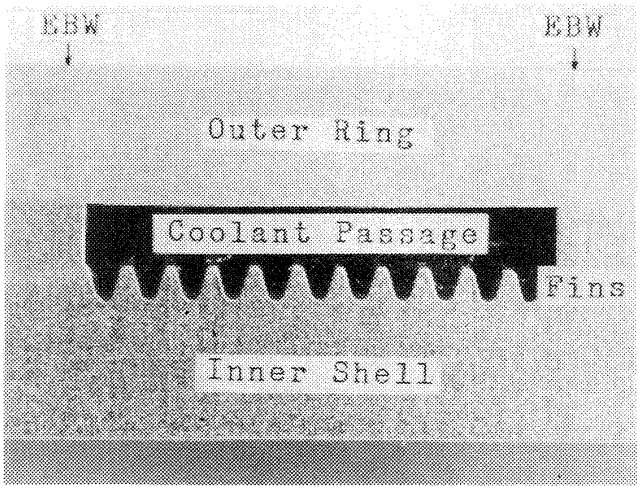

Fig. 8 Cooling channel

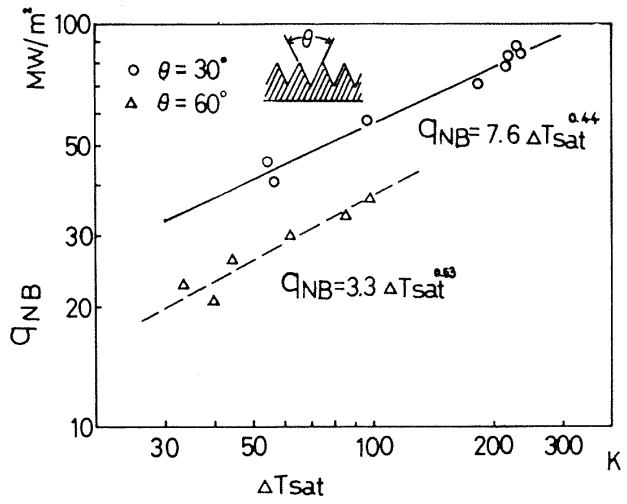

Fig. 9 Boiling heat transfer characteristics

coolant passages and their height were 1 mm. The heat fluxes measured under nucleate boiling of 30-degree fins were almost twice those of 60-degree fins (Ref. 10) at the same wall superheat.

2.3 Instrumentation

Five thermocouples were installed in the chamber wall through the land between the neighboring cooling channels to determine the hot gas side-wall temperature. The two wall thermocouples at the throat section consisted of a Chromel and Alumel wire 0.045 mm in diameter in a sheath made of 0.25 mm stainless steel tubing. The other thermocouples consisted of 0.09 mm Chromel/Constantan wire in a 0.5 mm sheath. Probes were fixed by high thermal conductive epoxy resin at the bottom of drilled holes located 1.0 mm from the hot gas side surface.

The temperatures of inlet and outlet water were measured by Chromel/Constantan thermocouples inserted in an inlet manifold and each outlet manifold.

The water flow rate of each channel was measured by a calibrated orifice and the each propellant flow rate was measured by a turbine flowmeter.

Five pressure transducers were mounted on the cooling channel outer rings to determine the saturation temperature in the cooling channels.

The thrust of the chamber was not measured because of the large quantity of rigid hardware mounted on the test assembly.

2.4 Test Facility

The setup consists of the fuel and oxidizer feed systems, a water coolant feed system, a thrust stand, the test hardware, the igniter feed systems, and the instrumentation.

A schematic diagram of the water-cooled combustion test facility is shown in Fig. 10. Liquid oxygen was

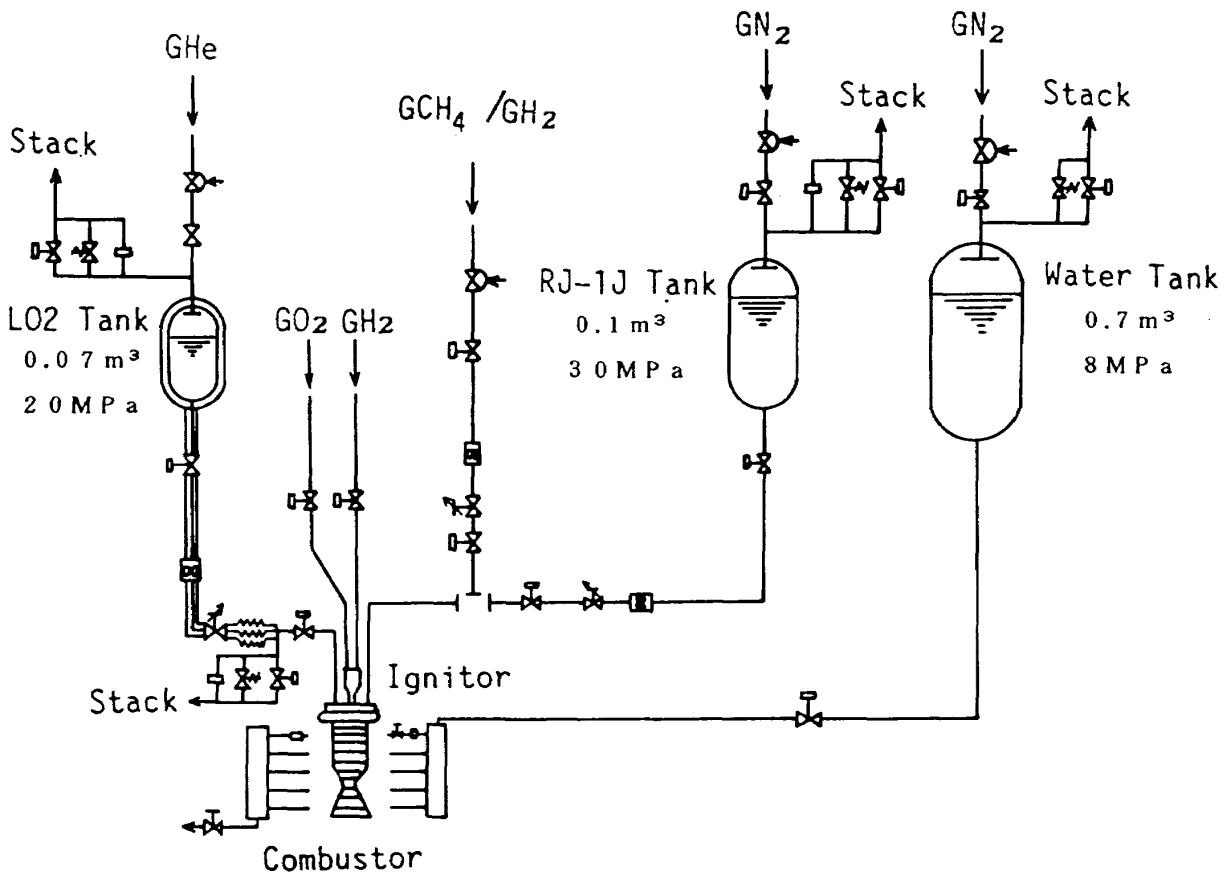

Fig. 10 Schematic diagram of test facility

supplied from a high pressure tank and pressurized by gaseous helium into the water-cooled main combustion chamber. Gaseous hydrogen or methane was fed from 20 MPa storage bottles. RJ-1J was also supplied from a high pressure tank pressurized by gaseous nitrogen. A preburner was installed in order to study the effects of hot gas injection through a simulaton of the staged combustion cycle of hydrogen or methane fuel. Details of the preburner assembly are shown in Ref. 8.

A torch igniter with a spark plug was used for ignition for LOX/gaseous hydrogen and LOX/gaseous methane combustion tests. The gaseous oxygen/gaseous hydrogen propellant was fed from high pressure bottles. Sonic venturis were used to control the flow rates. A power supply provided the required spark energy for ignition.

A pyrotechnic igniter was used for ignition of LOX/RJ-1J propellant.

2.5 Data Recording

All pressures, temperatures and flow rates were recorded in digital form at a rate of 100 Hz/second for each signal on a magnetic tape. After processing, all the original data and processed data were printed out at 0.1 second intervals.

The local heat flux was calculated from the temperature increase, the flow rate of the water, and the hot gas side surface area in each cooling channel.

3. TEST PROCEDURE AND CONDITIONS

3.1 Test Procedure

A programmable sequencer was used to control the test events. The fuel, oxidizer and water flow were set by a combination of tank pressures and openings of needle valve. The water flow rate of each channel was determined so as to obtain sufficient temperature increase for precise measurement under nucleation boiling conditions. An empirical equation (Ref. 10) obtained with 60-degree fins was used to predict the critical heat flux of 30-degree fins because of the lack of data.

The duration of the firing tests was long enough for the hot gas side wall temperature and outlet water

temperature to reach steady state. This condition was achieved in 15 to 30 seconds depending on the values of heat fluxes. The water flow, however, was commenced 15 seconds prior to ignition in order to achieve the inlet temperature steady state.

The tests were monitored by two television cameras and recorded by two video tape recorders for playback.

The chamber and the injector were inspected after each test and the diameter of the throat was measured for the reduction of the C* efficiency.

A number of emergency alrams and shut-off devices were incorporated to protect the system from accidental damage during operation. If these were tripped, secure and rapid shut-off was automatically achieved. The shut-down time of the propellant feed system was within 0.3 seconds. The items which could activate the alarms were the wall temperature, the hot gas temperature and mixture ratio of the preburner, and the level and pressure of the feed tanks. A few slow but important signals were registered on a pen recorder and shut-off was manually achieved when necessary.

3.2 Test Conditions

Firing tests were carried out, covering a combustion pressure range of 3.5 to 10.4 MPa and a sea level thrust range of 3 to 7 kN. Fig. 11 shows a photo of a firing test with LOX/RJ1-J propellants. Test conditions and the achieved C* efficiencies are summarized in Table 1. Details of the combusion characteristics of these propellants are shown in the references (Ref. 7–9). All heat transfer data cited are given in the appendix.

The short chamber was used in LOX/room temperature gaseous hydrogen, LOX/methane and LOX/RJ-1J combustion tests.

A crack due to low-cycle thermal fatigue was found after the tests. Fig. 12 shows photos of the cracked chamber wall. Staged combustion tests using the long chamber with 27 cooling channels were then conducted to achieve higher combustion efficiencies for LOX/hydrogen and LOX/methane propellants.

Table 1 Range of Test Conditions

Propellants	Number of Tests	Pc MPa	O/F	$T_{f,inj}$ K	ηC_* %
LOX/H_2	13+	7.1 - 9.5	4.8 - 6.9	280 - 990	96 - 100
LOX/CH_4	25+	3.5 - 9.6	2.7 - 5.1	270 -1100	89 - 99
LOX/RJ-1J	22	5.3 -10.4	1.8 - 3.4	275 - 285	95 - 100

+ Included staged combustion tests.

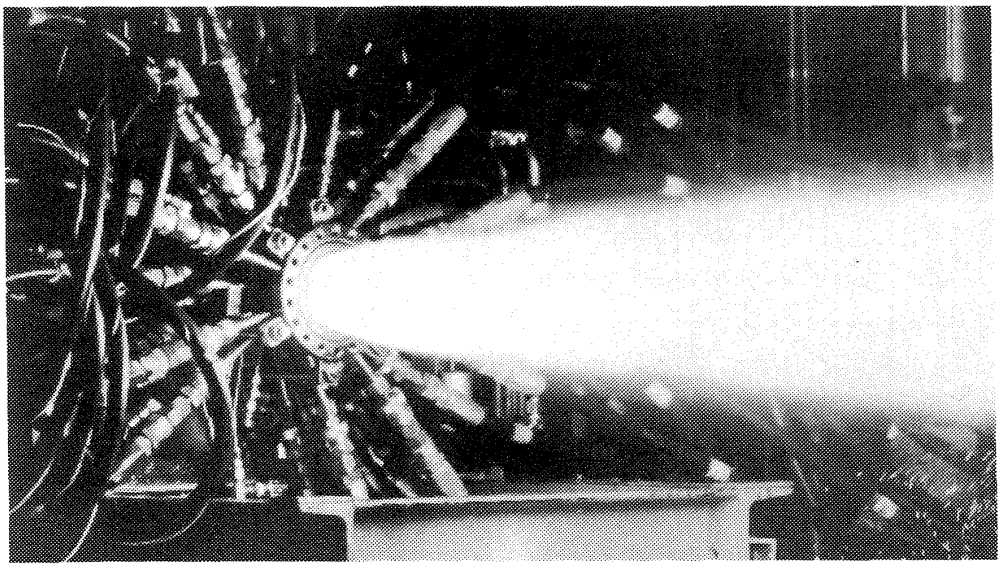

Fig. 11 Photograph of LOX/RJ-1J firing test

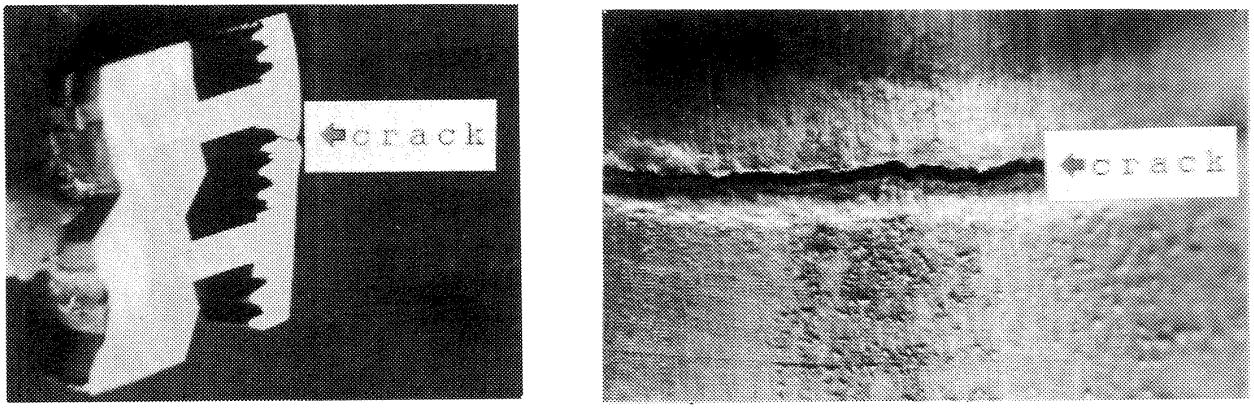

Fig. 12 Photograph of cracked chamber wall

4. TEST RESULTS

4.1 Heat Transfer Correlations

Due to the uncertain effects of hot gas side heat transfer on the thrust chamber, the simplified Bartz's equation (Ref. 11) has been commonly used to compare the test results of different propellants.

The present authors have previously proposed the application of the empirical correlation (Ref. 12) to account for the injector end effect on heat transfer near the injector end with coaxial elements as shown in Fig. 13 and Fig. 14. They also proposed the use of the empirical correlation (Ref. 12) of the effect of fuel film cooling from holes on the injector surface as shown in Fig. 15. These correlations were also used to predict heat flux distribution under the present test conditions using LOX/hydrogen and LOX/methane propellants.

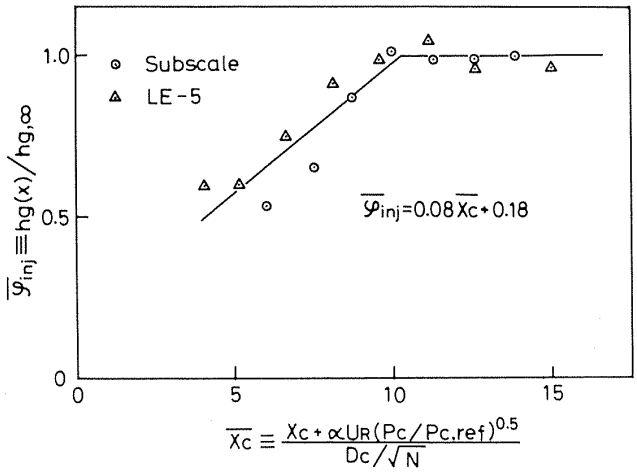

Fig. 13 Normalized injector end effect with non-dimensional distance from injector face

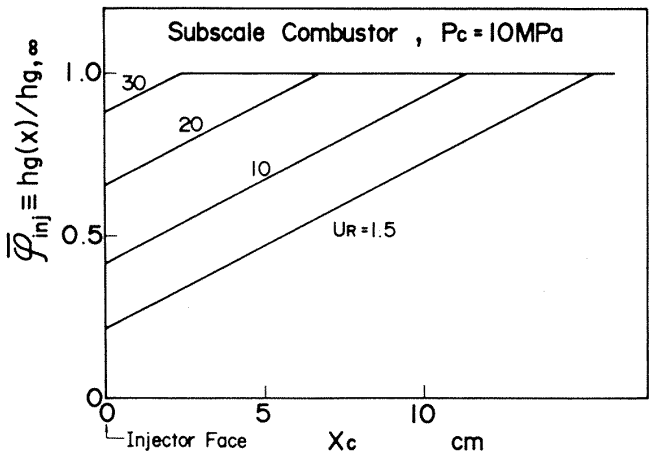

Fig. 14 Normalized injector end effect with various injection velocity ratios

4.2 Heat Transfer Characteristics of LOX/Hydrogen Propellants

Fig. 16 shows an example of LOX/room temperature hydrogen data versus time. The chamber pressure was around 9 MPa, and wall temperatures of the throat section and cylindrical section were quite stable after the start transient of 1 second. The outlet temperature of water at the throat section was also stable except at the start transition.

An example of axial heat flux distribution of LOX/room temperature hydrogen is shown in Fig. 17. The solid line in the figure is calculated by Bartz's original equation and the dotted line is calculated by the modified Bartz's equation which used the coefficient, Cg = 0.023, the same result as that of the Dittus-Boelter type of equation, as well as the injector end effect and the film

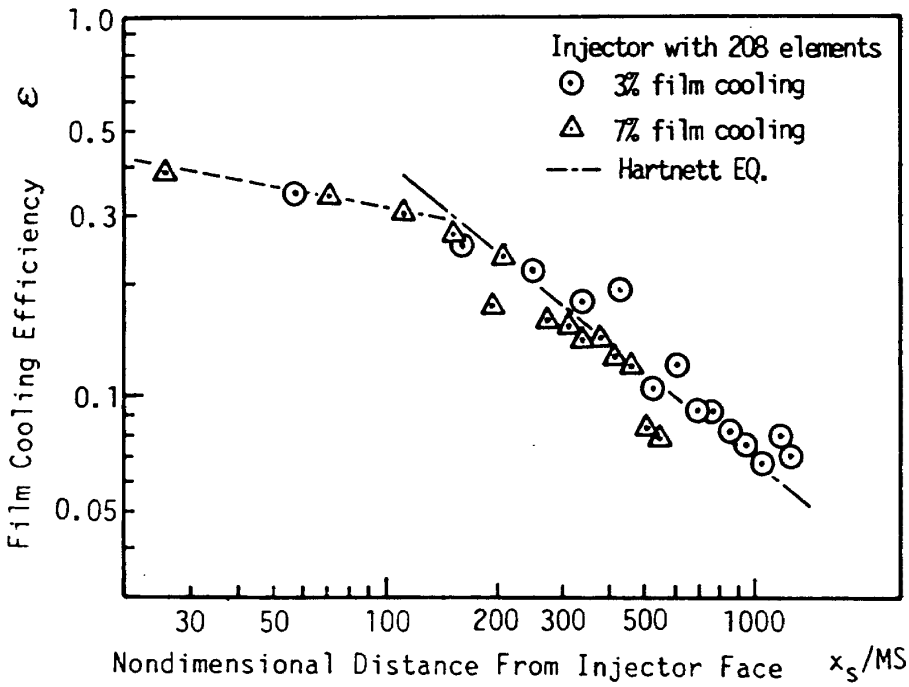

Fig. 15 Film cooling effect of LE-5 calorimetric chamber

cooling effect. The values predicted by the modified Bartz's equation agreed well with the measured values, although the predicted heat flux exceeded that of the one measured at the divergent section of the nozzle. At the divergent nozzle section, a different type of heat transfer equation, such as a boundary layer equation, might be applicable. The present discussion, however, is limited to the heat flux variations within the chamber and nozzle throat section.

Fig. 18 shows an example of LOX/hydrogen staged combustion data versus time. The main chamber pressure was around 9 MPa, and the temperature overshoot of the preburner was observed during start and shut down transient, it did not affect the measurement of wall temperatures or the outlet water temperatures. All of the measured temperatures were quite stable except the transient period.

An example of axial heat flux distribution of the LOX/hydrogen staged combustion test is shown in Fig. 19. The double-dot-dash-line was determined by the modified Bartz's equation which accounts for the injector end effect and the film cooling effect. Calculated values also agree with the measured values within the chamber though the location of the measured maximum heat flux shifted upstream a little.

4.3 Heat Transfer Characteristics of LOX/Methane Propellants

Fig. 20 shows an example of LOX/room temperature methane data versus time. The chamber pressure was around 7 MPa and decreased slightly during combustion. This was caused by partial flow blockage in the rigimesh faceplate of the injector or the needle valve port due to ice formation, because methane fuel included a slight amount of water vapor. As a result, the wall temperature of the throat section and that of the cylindrical section decreased during combustion. However, the outlet temperature of water at the throat section was not greatly affected.

Two axial heat flux distributions in tests using LOX/methane propellants are shown in Fig. 21. The measured values of heat flux of the 6.9 MPa test which used room temperature methane are shown as circles in the figure. The double-dot-dash-line was determined by the modified Bartz's equation which accounted for the injector end effect and the film cooling effect. The dotted line was determined by the same equation, but included only the injector end effect. The experimental value is in approximate agreement with the double-dot-dash-line at the location $x < -30$ mm from the nozzle throat and in agreement with the dotted line at $-30\text{ mm} < x < 0$ mm. This indicates that the film cooling effect does not

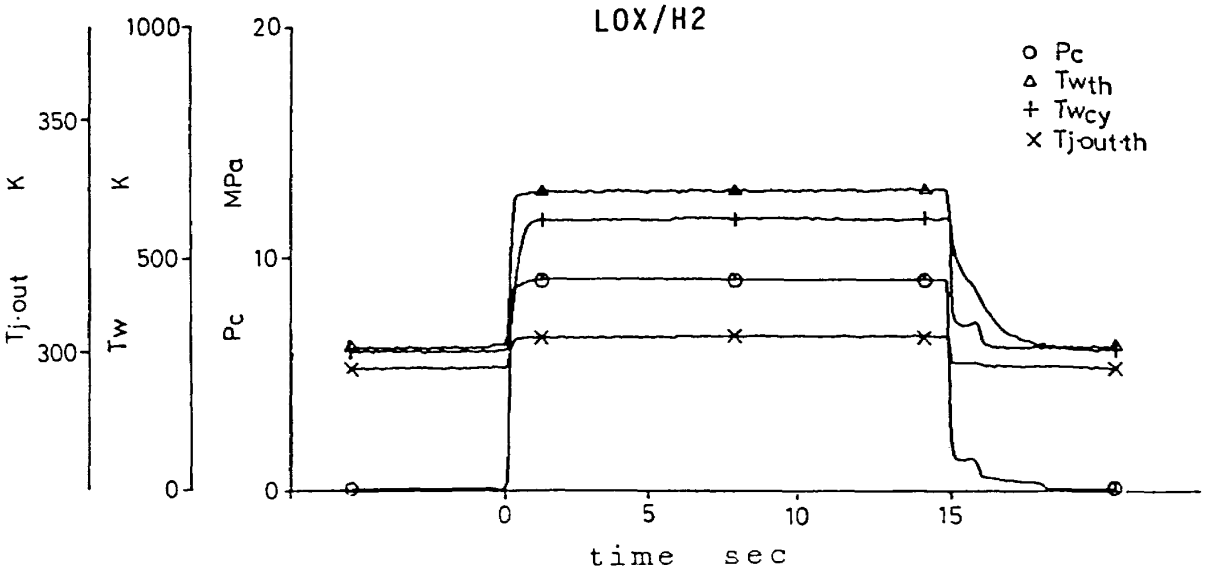

Fig. 16 LOX/room temperature hydrogen data vs. time

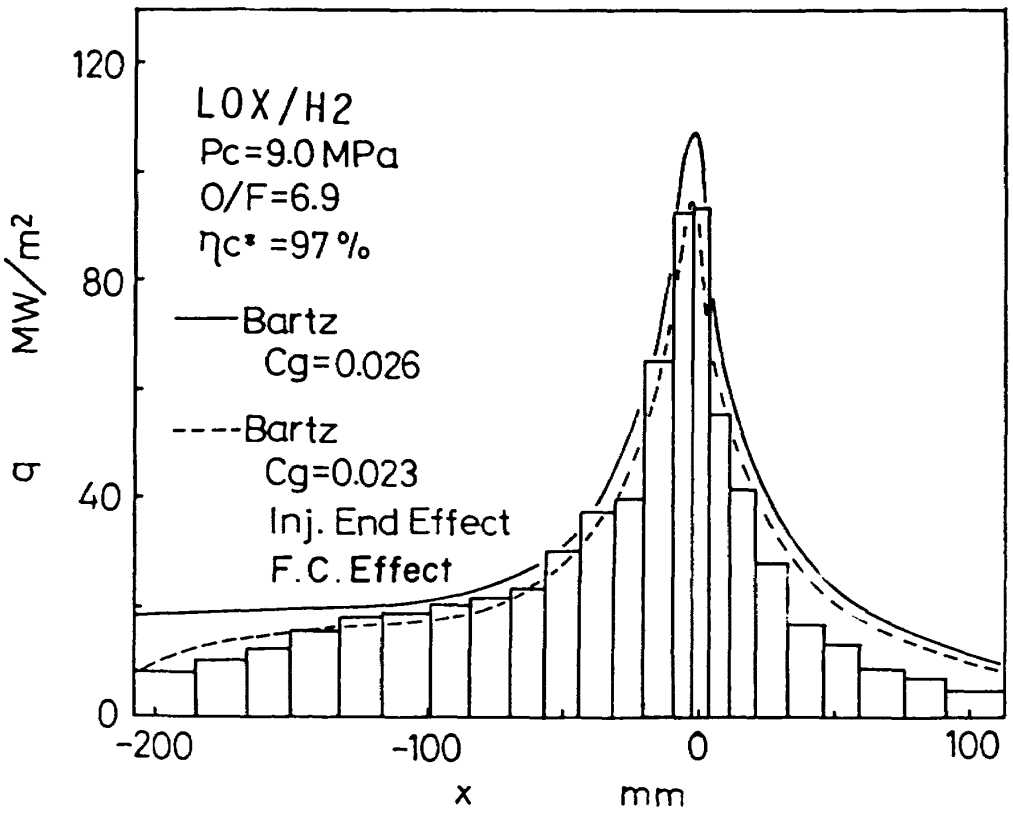

Fig. 17 Heat flux distribution of LOX/room temperature hydrogen

apparently occur around the throat section.

Fig. 22 shows an example of LOX/methane staged combustion data versus time. The main chamber pressure was around 9.6 MPa, but the decrease of the pressure shown in Fig. 20 was not observed in this case. A large temperature overshoot of the preburner was observed during the start transient. All of the measured temperatures were quite stable except during the transient period.

A typical result of the 9.6 MPa staged combustion test, using the injector without film cooling holes, is also shown by squares in Fig. 21. The single-dot-dash-line was determined by the modified Bartz's equation, accounting for the injector end effect. The experimental values were also in approximate agreement with the value

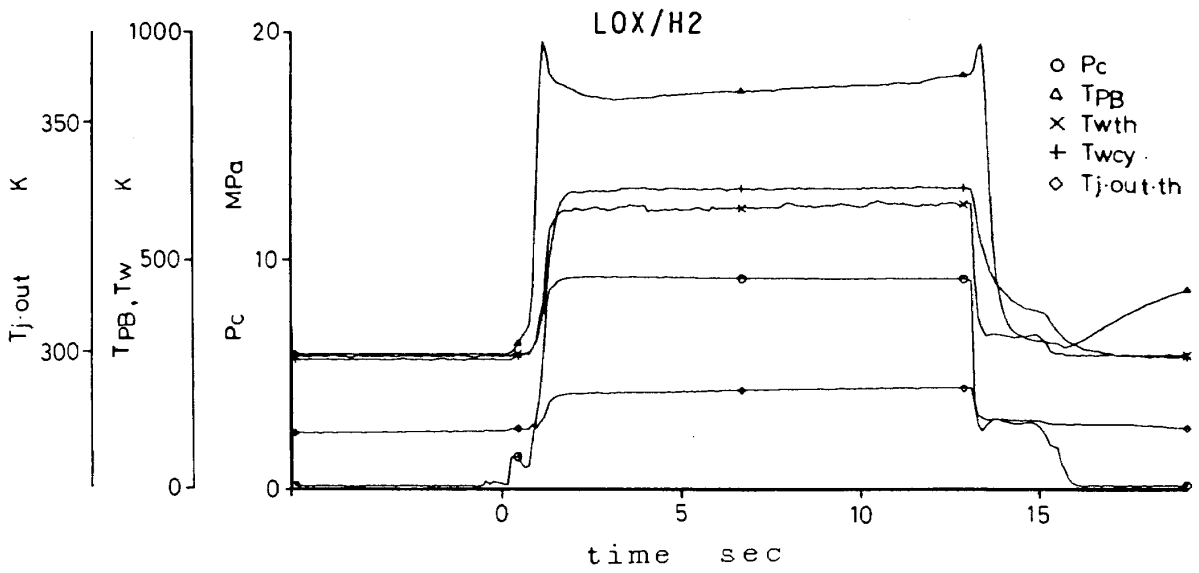

Fig. 18 LOX/hydrogen staged combustion data vs. time

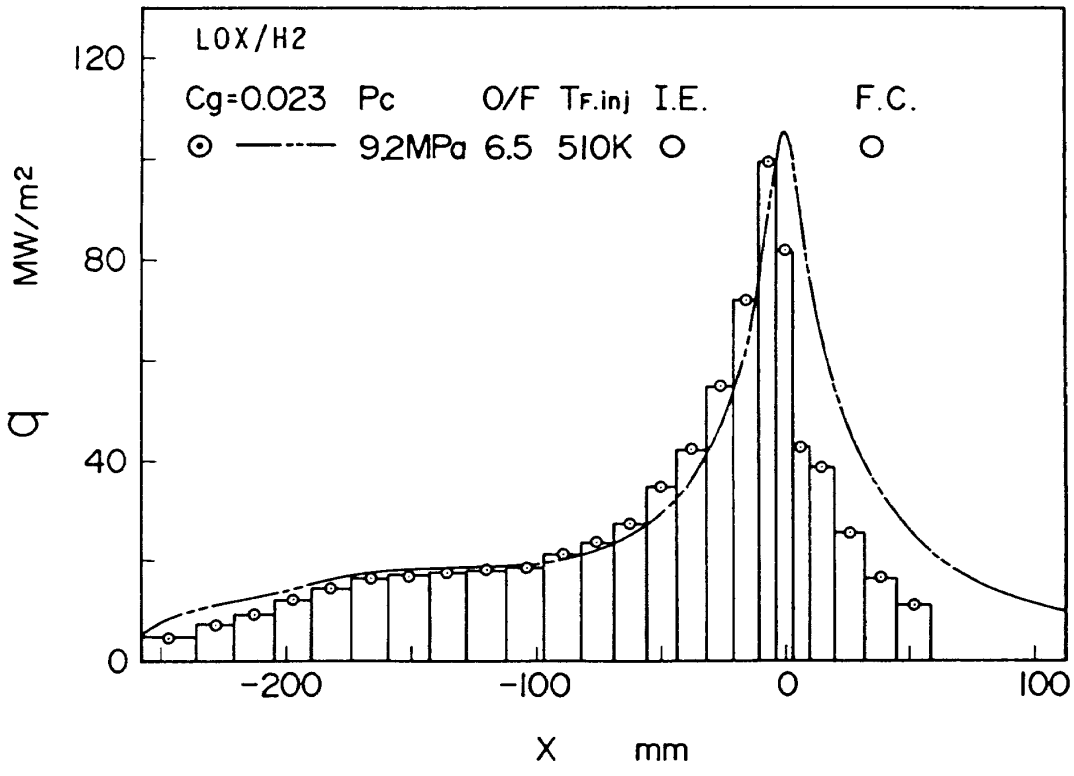

Fig. 19 Heat flux distribution of LOX/hydrogen staged combustion test

predicted for the area between the cylindrical section and the nozzle throat section.

After the firing test, a thin, fragile deposition of soot on the wall was observed; there was no remarkable evidence of a heat flux level less than the one predicted by the modified Bartz's equation. It was therefore concluded that the carbon layer which developed during the combustion tests using LOX/methane propellants did not have any effect on the heat transfer.

4.4 Heat Transfer Characteristics of LOX/RJ-1J Propellants

Fig. 23 shows data plots of LOX/RJ-1J propellant with the FOF injector. The chamber pressure was around 10 MPa. No chamber pressure overshoot was observed during start and shut down transient. Though the measured

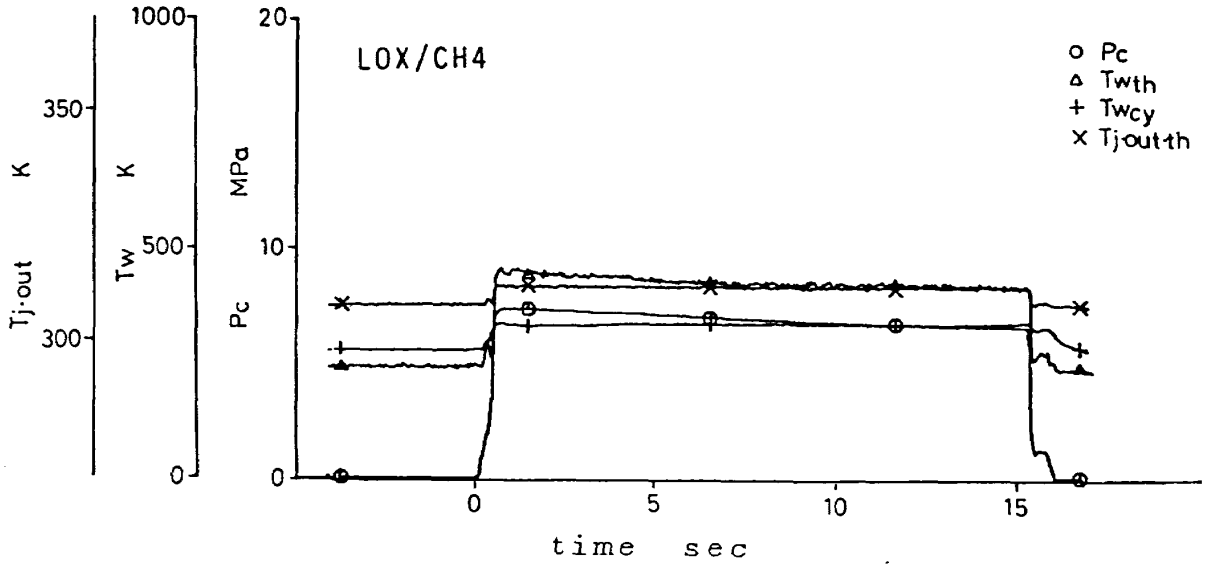

Fig. 20 LOX/room temperature methane data vs. time

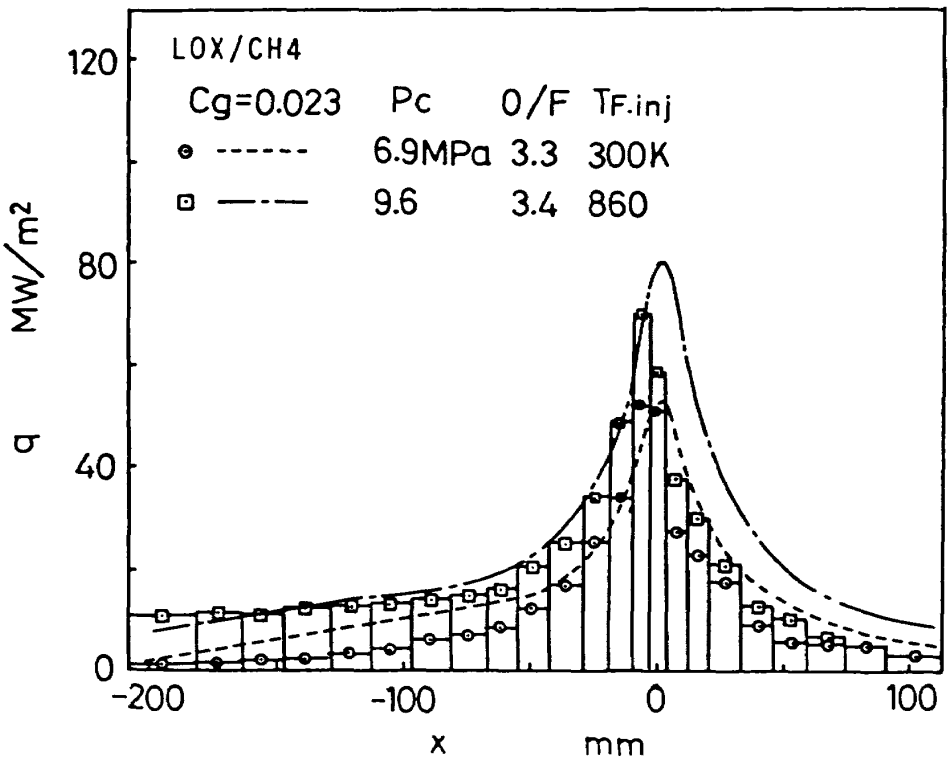

Fig. 21 Heat flux distribution of LOX/methane

exit water temperatures were quite stable except duimg the transient periods, the wall temperatures varied cyclically. The wall temperature variation with time was thought to be caused by carbon deposit buildup and spalling on the chamber wall. Such variation was not observed in the case of LOX/methane propellant.

Fig. 24 shows two examples of the axial heat flux distribution of LOX/RJ-1J propellants. The heat fluxes measured in the FOF injector were lower than those calculated by the modified Bartz's equation with the coefficient Cg = 0.023, which was valid in the cases of LOX/hydrogen and LOX/methane propellants. It is inferred that the soot deposition on the wall decreased heat flux to the entire wall especially at lower mixture ratios

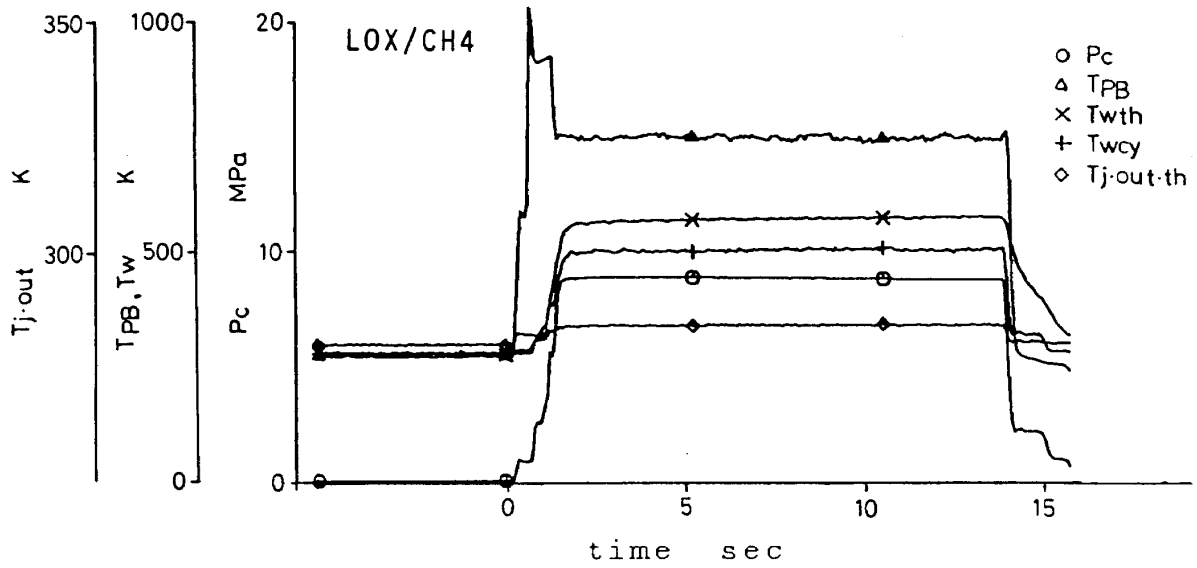

Fig. 22 LOX/methane staged combustion data vs. time

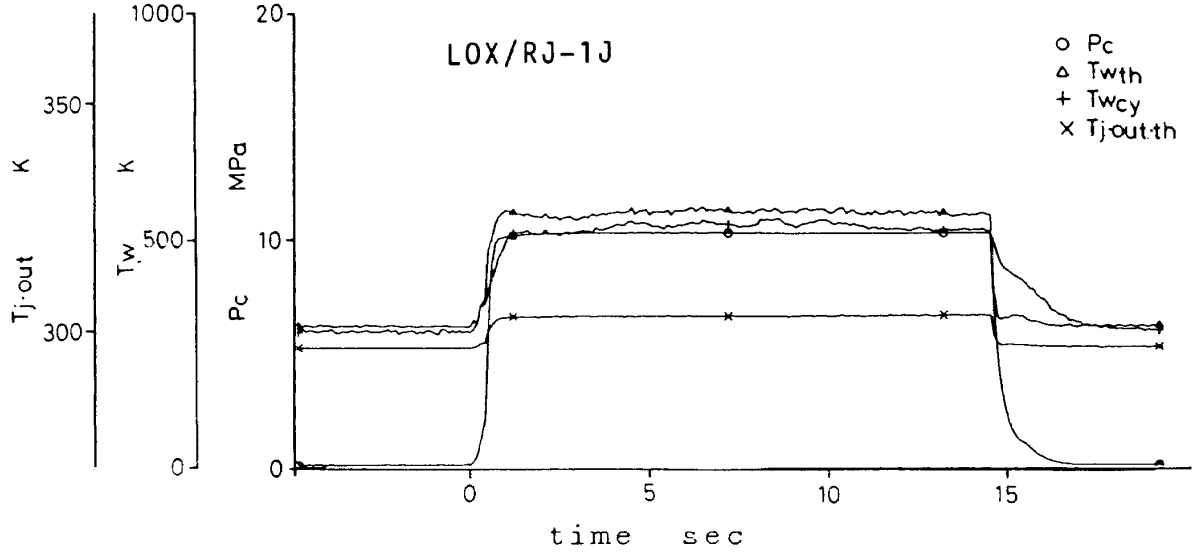

Fig. 23 LOX/RJ-1J data vs. time

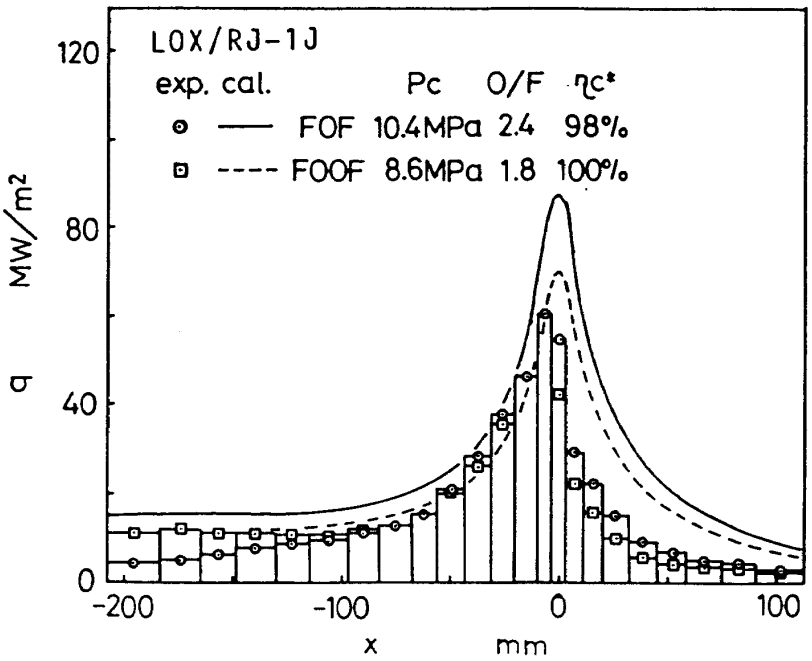

Fig. 24 Heat flux distribution of LOX/RJ-1J

and also that the injector end effect, similar to that of the coaxial element injector, decreased heat flux near the injector end.

High frequency combustion instability occurred in the case of the FOOF injector when the cavity ring was not installed, and the injector faceplate made of copper was found damaged after the test because the injector surface had not been protected with transpiration cooling. Heat fluxes at the cylindrical section were higher than those analogized from the heat flux distribution in the FOF injector, as shown in Fig. 24, and were in approximate agreement with those obtained by the modified Bartz's equation.

4.5 Effects of Chamber Pressure

The highest heat flux for each test was plotted as a function of combustion chamber pressure, as shown in Fig. 25. The maximum heat flux predicted by Bartz's equation (Cg = 0.026), which employed average combustion efficiency of each propellant, is also plotted in the figure. In the case of LOX/hydrogen, experimental values were about 85 to 90% of those of predicted values. On the other hand, they were about 70 to 90% in the case of LOX/methane and about 60 to 90% in the case of LOX/RJ-1J. The lower values for LOX/methane propellants were mainly due to the lower combustion efficiencies achieved. The wide scatter in the case of LOX/RJ-1J propellants was supposed due to soot deposition on the wall. Therefore, the effect of soot deposition was examined in results of LOX/RJ-1J propellants.

4.6 Soot Observation

After a series of firing tests with LOX/RJ-1J propellants, using the FOF type of injector, a carbon layer was fixed by epoxy resin near the injector end and the nozzle end, and a sample from each of these respective sections was removed from the wall intact. Fig. 26 shows SEM (Scanning Electron Microscope) photographs of the sections and the structures of the carbon layer in both samples. The thickness of the carbon layer near the injector end was about 15 microns and that of the layer near the nozzle end was about 20 microns. The layer near the injector end had a smooth and marbled structure. The layer near the nozzle end was composed of particle lumps. The mechanism of soot formation and the deposition mechanism of the carbon layer remain to the clarified in future studies.

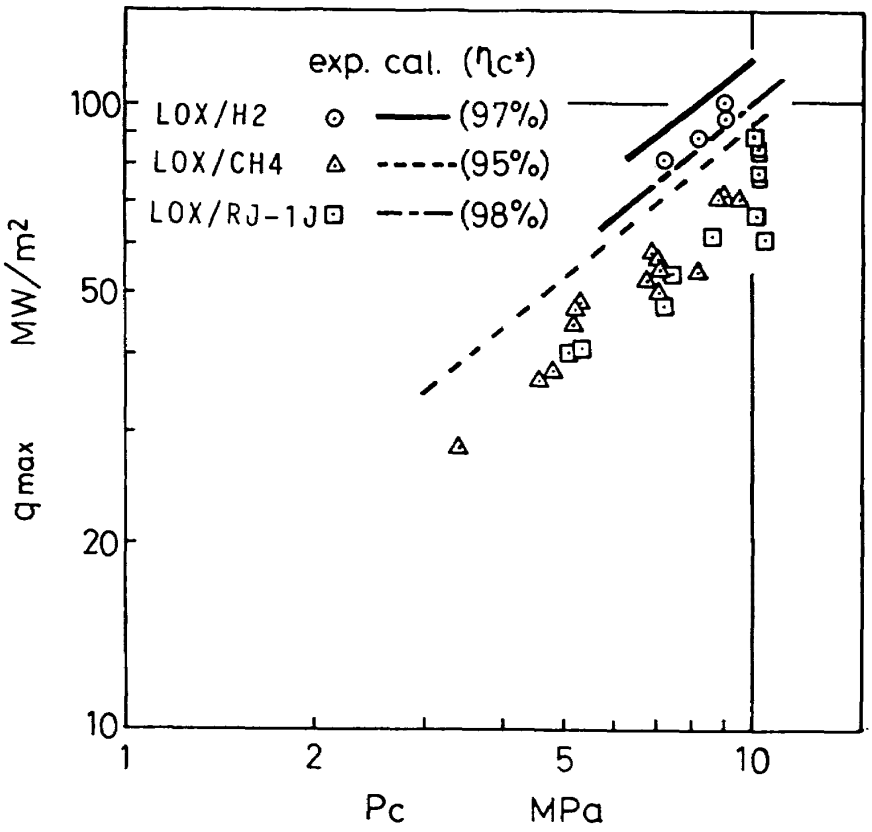

Fig. 25 Measured maximum heat flux as a function of chamber pressure

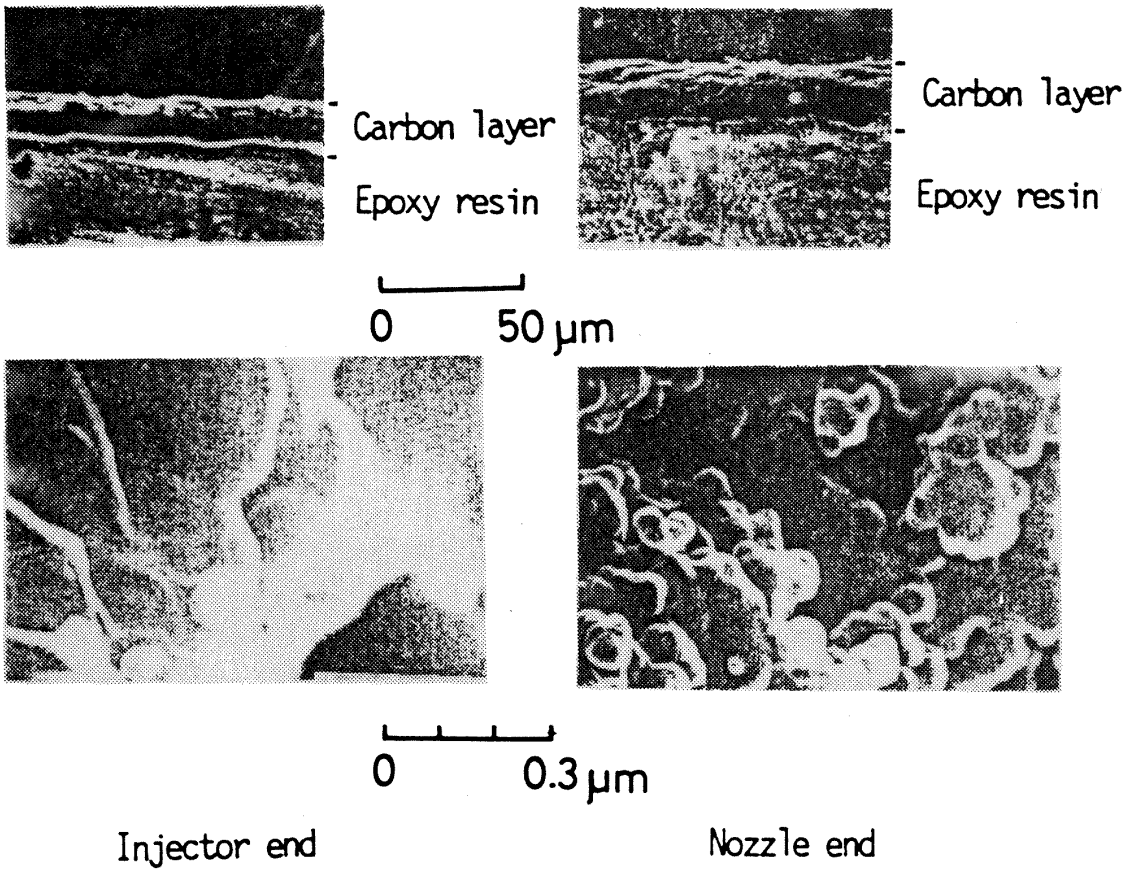

Fig. 26 Photos of the soot of LOX/RJ-1J

4.7 Soot Resistance Correlations

The carbon deposition on the chamber walls in the case of LOX/hydrocarbon propellants was studied in the literature (Ref. 13–15). Hernandez et al. (Ref. 13) gave a brief overview of the carbon deposition and reported that no carbon deposition was, however, detected under high combustion pressures of the main chamber. The classical "g-model" empirical correlation used to predict the thermal resistance of the carbon layer is described in Ref. 14. Price et al. (Ref. 15) reported that carbon deposition was detected on the liquid oxygen cooled chamber walls when LOX/RP-1 was used as the propellant.

Carbon deposition on the chamber walls is a very complicated phenomenon. Existing data trends are shown in Fig. 27 and several correlations are summarized in Ref. 13.

The thermal resistance tc/kc of the carbon layer in the case LOX/RP-1 was correlated with the combustion gas mass flux G, as shown in Fig. 28 (Ref. 14). The dotted line shows the empirical correlation previously suggested for the design of the LOX/RP-1 combination in the 1960s (Ref. 14). In this study, the injector having 10% film cooling caused high thermal resistance of carbon deposition layer due to incomplete combustion near the wall.

Price et al (Ref. 15) discussed the thermal resistance of carbon deposition but didn't correlate it with the combustion gas mass flux. The present author deduced thermal resistance based on the reported data as shown in Fig. 29. The injector used in Ref. 15 had an impinging pattern in the inner zone, a showerhead pattern in the outer zone and no film cooling. Therefore, the mixture ratio in the outer zone of the injector, being lower than the overall mixture ratio, caused a lower combustion temperature and incomplete combustion near the wall. Though the absolute values of thermal resistance differ in both these studies, they agree in that thermal resistance decreased when mass flux increased.

The existing classicial "g-model", also recommended in Ref. 13, was chosen to compare the present data with the previous data.

The thermal resistance in the present study is plotted

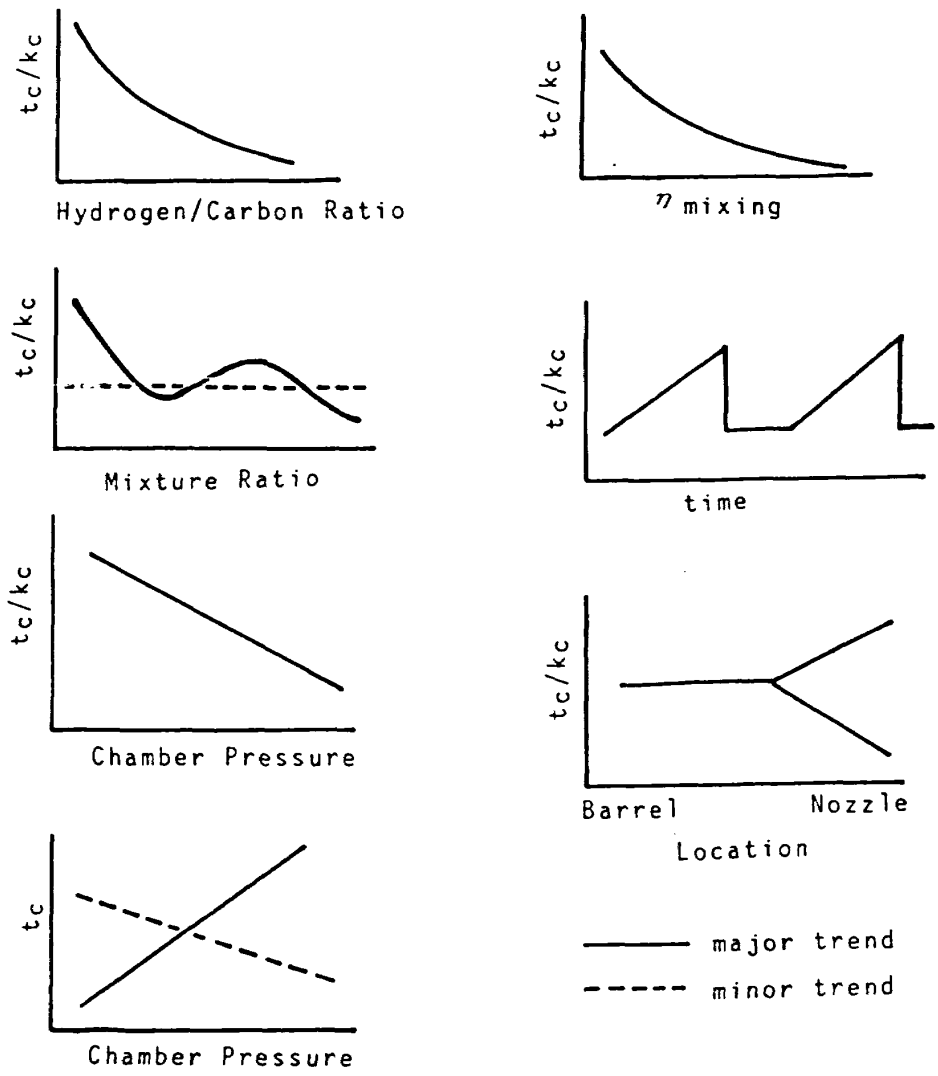

Fig. 27 Carbon deposition trends (Ref. 13)

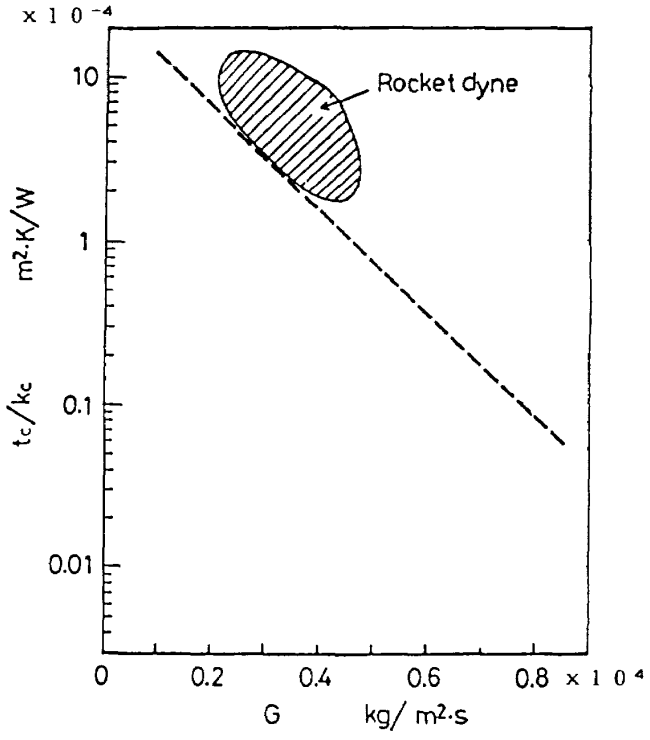

Fig. 28 Thermal resistance of the carbon layer (Ref. 14)

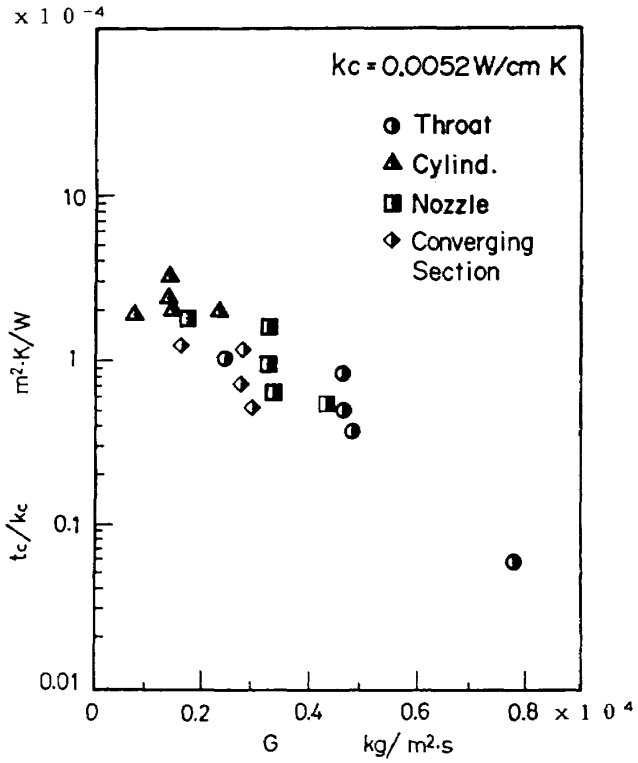

Fig. 29 Thermal resistance of the carbon layer (Ref. 15)

in Fig. 30. The circles in the figure indicate the thermal resistance that was deduced from the difference between the levels of heat flux in the modified Bartz's equation and the actual values measured at the throat section. The two black dots indicate the thermal resistance deduced from the thickness of the layer in Fig. 26 and the thermal conductivity of soot that was cited from an earlier study (Ref. 15) as a constant value of kc = 0.52 W/mK. Data derived from two earlier studies (Ref. 14 and 15) are also shown in Fig. 30. The thermal resistances at the same mass flux in these two previous studies were higher than that in the present study which used an injector with a uniform impinging pattern, and employed no film cooling. Though the absolute values of thermal resistance differ in these studies, they agree in that thermal resistance decreased when mass flux increased.

To obtain a minimum value of thermal resistance at the same mass flux for practical use, an empirical correlation was calculated by connecting the experimental minimum values of thermal resistance shown as a solid line in Fig. 30. The slope of the dotted line, which indicates a previous design equation, is equal to that of the solid line. However, the absolute value of thermal resistance obtained in this study is a small percentage of that of the previous correlation. Thus heat flux reduction due to carbon deposition is not expected to occur to the same degree in the case of a high performance injector without film cooling holes. This expectation derives from the higher mass flux: i.e., combustion chamber pressure is higher and the location is closer to the throat section with the highest heat flux.

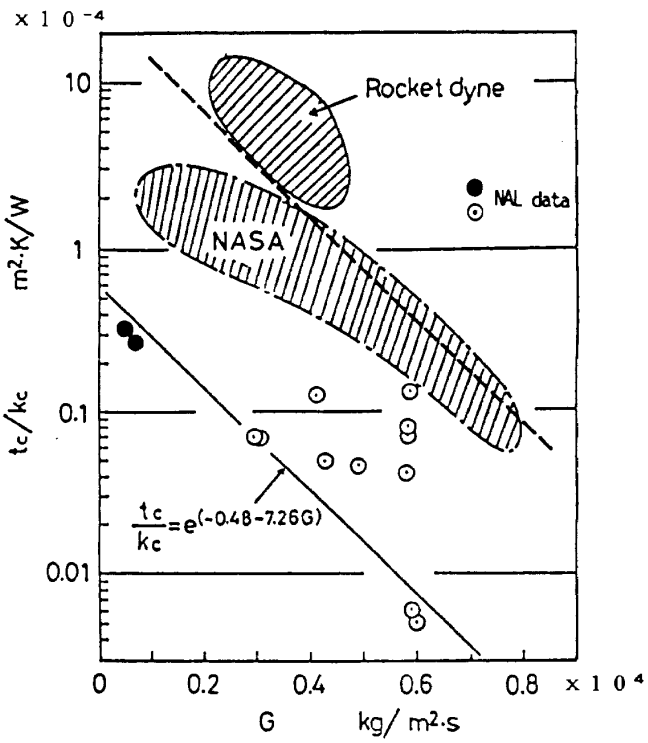

Fig. 30 Comparison of thermal resistance of the carbon layer with different data

5. SUMMARY

(1) Combustion tests using liquid oxygen (LOX)/gaseous hydrogen, LOX/gaseous methane and LOX/RJ-1J as propellants were conducted. Two types of water cooled calorimetric combustors and two types of injectors, a coaxial and an impinging injector, were employed. The chamber pressure was as high as 10 MPa and the heat flux reached 100 MW/m^2.

(2) Heat flux values measured at the throat section were lower than those predicted by the simplified Bartz's equation. The modified Bartz's equation, which used 0.023 as a coefficient instead of the 0.026 of the original, and which takes into account the injector end effect as well as the film cooling effect, more accurately predicted the heat flux distribution measured in a coaxial type injector.

(3) In cases where LOX/RJ-1J propellants using the FOF type of injector without film cooling holes were employed, an empirical correlation for the thermal resistance of a carbon layer deposited on the chamber wall was obtained. It was observed that the values of thermal resistance measured were a small percentage of the values found in previously published data.

ACKNOWLEDGEMENTS

The authors wish to acknowledge their debt to Dr. E. Armstrong of NASA/Lewis who helped to correlate the referred data of the late Dr. H.G. Price, and also to those at Tokyo Gas Co., Ltd., Technology Research Institute, who cooperated with the authors on the occasion of the SEM observations. They also wish to acknowledge that a part of the data cited in this study was obtained through joint research with the National Space Development Agency of Japan as well as Ishikawajima-Harima Heavy Industries Co., Ltd.

REFERENCES

1. Talay, T.A., "Shuttle 2", SAE Paper 87-1335, 1987.
2. Martin, J.A., "Two-Stage Earth-to-Orbit Vehicles with Series and Parallel Burn", AIAA Paper 86-1413, 1987.
3. Martin, J.A., "Space Transportation Main Engines for Single-Stage Vehicles", AIAA Paper 87-1941, 1987.
4. Schmidt, G., "Study on Rocket Engines for Future European Launchers", SEP TPRL/K N19572/84, 1984.
5. Schibato, Y., "Study on Future Space Transportation Vehicles", proceedings of the 19th Workshop on Technological Progress of NASDA, 1987, pp. 39.
6. Pavli, A.J., "Design and Evaluation of High Performance Rocket Engine Injectors for Use with Hydrocarbon Fuels", NASA TM-79319, 1979.
7. Yatsuyanagi, N., et al., "Experimental Study on the LO2/Hydrogen Staged Combustion Rocket Engine, Part 2: Main Burner", 14th Int. Symposium on Space Tech. & Sci., Tokyo, 1984.
8. Tamura, H., et al., "LOX/Methane Staged Combustion Rocket Combustor Investigation", AIAA Paper 87-1856, 1987.
9. Tamura, H., et al., "High Pressure LOX/Heavy Hydrocarbon Fuel Rocket Combustor Investigation", 16th Int. Symposium on Space Tech. & Sci., Sapporo, 1988.
10. Niino, M., et al., "A Study on Heat Transfer Characteristics of Water Cooled LO2/LH2 Rocket Combustor", NAL TR-708, 1982.
11. Bartz, D.R., "A Simple Equation for Rapid Estimation of Rocket Nozzle Convective Heat Transfer Coefficients", Jet Propulsion, 27, (1), 49-51, 1957.
12. Niino, M., et al., "Similarity of LOX/LH2 Rocket Combustors", NAL TR-767, 1983.
13. Hernandez, R., et al., "Carbon Deposition Model for Oxygen-Hydrocarbon Combustion", NASA CR-179375, 1987.
14. Cook, R.T., "Advanced Cooling Techniques for High-Pressure Hydrocarbon-Fueled Engines", NASA CR-159790, 1979.
15. Price, H.G., et al., "Liquid Oxygen Cooling of High Pressure LOX/Hydrocarbon Rocket Thrust Chambers", NASA TM-88805, 1986.

APPENDIX

(1) LOX/H2 Test Results

RUN 572

Pc = 7.12 MPa, O/F = 5.96, Mt = 1.27 kg/s, Tf = 303 K, $\eta c^* = 99.6\%$

Segment No.	q, exp MW/m^2	Segment No.	q, exp MW/m^2
1	7.6	13	53.0
2	9.2	14	76.6
3	10.7	15	80.2
4	13.6	16	45.6
5	15.4	17	37.0
6	16.1	18	23.6
7	16.6	19	14.1
8	18.2	20	11.3
9	19.0	21	7.4
10	23.4	22	6.0
11	30.3	23	3.9
12	30.8		

RUN 573

Pc = 9.32 MPa, O/F = 6.17, Mt = 1.65 kg/s, Tf = 298 K, $\eta c^* = 96.7\%$

Segment No.	q, exp MW/m^2	Segment No.	q, exp MW/m^2
1	8.2	13	65.5
2	10.3	14	93.8
3	12.1	15	92.8
4	15.4	16	52.8
5	17.7	17	42.6
6	18.6	18	27.8
7	19.8	19	16.7
8	21.6	20	13.1
9	23.7	21	8.5
10	29.4	22	6.9
11	38.0	23	4.6
12	49.4		

RUN 574

Pc = 9.08 MPa, O/F = 5.67, Mt = 1.60 kg/s, Tf = 303 K, $\eta c^* = 98.2\%$

Segment No.	q, exp MW/m^2	Segment No.	q, exp MW/m^2
1	8.6	13	68.0
2	11.1	14	99.0
3	12.9	15	96.5
4	16.4	16	53.0
5	18.4	17	42.8
6	19.2	18	28.8
7	21.0	19	17.3
8	22.3	20	13.7
9	24.2	21	8.8
10	31.6	22	6.9
11	38.6	23	4.7
12	45.4		

RUN 575

Pc = 8.96 MPa, O/F = 6.86, Mt = 1.68 kg/s, Tf = 300 K, $\eta c^* = 96.9\%$

Segment No.	q, exp MW/m^2	Segment No.	q, exp MW/m^2
1	8.0	13	65.3
2	10.1	14	92.8
3	11.8	15	93.4
4	15.4	16	52.8
5	17.5	17	41.7
6	18.5	18	28.2
7	20.2	19	16.8
8	21.7	20	13.2
9	23.1	21	8.6
10	30.2	22	6.9
11	37.4	23	4.7
12	39.8		

RUN 576

Pc = 8.14 MPa, O/F = 6.36, Mt = 1.48 kg/s, Tf = 298 K, $\eta c^* = 98.1\%$

Segment No.	q, exp MW/m^2	Segment No.	q, exp MW/m^2
1	7.7	13	61.0
2	9.8	14	87.3
3	11.5	15	87.7
4	15.0	16	49.3
5	16.8	17	39.6
6	17.7	18	26.7
7	19.1	19	15.7
8	20.4	20	12.5
9	21.5	21	8.1
10	28.1	22	6.7
11	35.0	23	4.4
12	47.7		

RUN 577

Pc = 9.50 MPa, O/F = 5.13, Mt = 1.68 kg/s, Tf = 888 K, $\eta c^* = 96.7\%$

Segment No.	q, exp MW/m²	Segment No.	q, exp MW/m²
1	16.9	15	37.7
2	20.3	16	48.9
3	20.1	17	65.4
4	20.2	18	87.6
5	19.9	19	75.4
6	19.7	20	49.5
7	19.0	21	37.4
8	18.7	22	24.6
9	18.8	23	14.9
10	18.6	24	10.4
11	20.4	25	–
12	22.5	26	–
13	24.6	27	–
14	31.5		

RUN 578

Pc = 8.73 MPa, O/F = 4.77, Mt = 1.53 kg/s, Tf = 936 K, $\eta c^* = 96.8\%$

Segment No.	q, exp MW/m²	Segment No.	q, exp MW/m²
1	17.0	15	34.3
2	20.9	16	44.8
3	20.3	17	59.1
4	19.8	18	79.5
5	18.9	19	66.1
6	18.5	20	42.5
7	17.7	21	33.8
8	17.4	22	21.4
9	17.2	23	13.6
10	17.0	24	9.0
11	19.0	25	–
12	20.7	26	–
13	23.0	27	–
14	29.2		

RUN 581

Pc = 9.15 MPa, O/F = 6.71, Mt = 1.72 kg/s, Tf = 782 K, $\eta c^* = 96.0\%$

Segment No.	q, exp MW/m²	Segment No.	q, exp MW/m²
1	15.2	15	42.5
2	18.0	16	55.3
3	18.5	17	71.9
4	19.2	18	91.8
5	19.6	19	80.3
6	20.0	20	–
7	19.2	21	35.5
8	19.5	22	25.8
9	19.2	23	16.7
10	19.2	24	11.9
11	22.0	25	–
12	24.4	26	–
13	27.4	27	–
14	35.2		

RUN 583

Pc = 9.24 MPa, O/F = 6.50, Mt = 1.71 kg/s, Tf = 511 K, $\eta c^* = 96.6\%$

Segment No.	q, exp MW/m²	Segment No.	q, exp MW/m²
1	4.9	15	42.0
2	7.3	16	54.7
3	9.2	17	71.9
4	12.1	18	99.1
5	14.7	19	81.5
6	16.5	20	42.8
7	17.1	21	38.4
8	17.7	22	25.5
9	18.0	23	16.4
10	18.7	24	11.1
11	21.2	25	–
12	23.8	26	–
13	27.1	27	–
14	34.8		

RUN 584

Pc = 9.26 MPa, O/F = 6.50, Mt = 1.71 kg/s, Tf = 516 K, $\eta c^* = 97.0\%$

Segment No.	q, exp MW/m^2	Segment No.	q, exp MW/m^2
1	4.0	15	42.1
2	6.3	16	55.7
3	8.5	17	72.5
4	11.4	18	99.9
5	14.0	19	86.7
6	16.1	20	50.3
7	16.9	21	39.3
8	17.7	22	26.0
9	18.0	23	16.3
10	18.7	24	11.2
11	21.2	25	–
12	23.8	26	–
13	27.2	27	–
14	35.8		

(2) LOX/CH4 Test Results

RUN 26

Pc = 3.51 MPa, O/F = 4.11, Mt = 0.86 kg/s, Tf = 286 K, $\eta c^* = 95.1\%$

Segment No.	q, exp MW/m^2	Segment No.	q, exp MW/m^2
1	3.1	13	17.1
2	3.6	14	25.4
3	3.9	15	28.5
4	4.7	16	18.9
5	4.9	17	14.1
6	6.0	18	9.7
7	6.0	19	5.9
8	6.1	20	4.5
9	6.7	21	3.2
10	8.3	22	2.7
11	9.7	23	1.7
12	13.0		

RUN 27

Pc = 4.54 MPa, O/F = 4.86, Mt = 1.16 kg/s, Tf = 283 K, $\eta c^* = 95.1\%$

Segment No.	q, exp MW/m^2	Segment No.	q, exp MW/m^2
1	4.5	13	25.4
2	4.7	14	36.3
3	4.6	15	32.1
4	5.2	16	14.9
5	5.4	17	42.6
6	6.0	18	10.8
7	6.1	19	6.6
8	6.9	20	4.9
9	7.4	21	3.4
10	9.6	22	2.9
11	11.4	23	1.9
12	16.8		

RUN 28

Pc = 4.62 MPa, O/F = 5.06, Mt = 1.23 kg/s, Tf = 280 K, $\eta c^* = 91.3\%$

Segment No.	q, exp MW/m^2	Segment No.	q, exp MW/m^2
1	3.7	13	24.9
2	4.8	14	37.8
3	5.2	15	35.6
4	5.8	16	21.5
5	5.8	17	16.3
6	6.6	18	11.5
7	6.3	19	6.9
8	7.4	20	5.2
9	8.1	21	3.6
10	10.9	22	3.0
11	13.3	23	2.0
12	19.2		

RUN 29

Pc = 5.23 MPa, O/F = 2.72, Mt = 1.27 kg/s, Tf = 278 K, $\eta c^* = 90.6\%$

Segment No.	q, exp MW/m^2	Segment No.	q, exp MW/m^2
1	4.9	13	33.8
2	5.7	14	47.4
3	6.0	15	42.6
4	6.9	16	26.8
5	6.8	17	19.5
6	6.9	18	13.8
7	8.1	19	8.5
8	9.6	20	6.2
9	10.6	21	4.3
10	14.3	22	3.6
11	17.8	23	2.3
12	25.7		

RUN 30

Pc = 5.11 MPa, O/F = 3.21, Mt = 1.27 kg/s, Tf = 278 K, $\eta c^* = 90.6\%$

Segment No.	q, exp MW/m^2	Segment No.	q, exp MW/m^2
1	4.1	13	27.9
2	5.4	14	39.8
3	5.8	15	35.7
4	6.6	16	23.0
5	6.7	17	18.2
6	7.3	18	11.9
7	7.4	19	7.4
8	8.1	20	5.4
9	9.0	21	3.8
10	12.0	22	3.2
11	15.1	23	2.0
12	20.8		

RUN 32

Pc = 5.36 MPa, O/F = 2.91, Mt = 1.31 kg/s, Tf = 272 K, $\eta c^* = 90.5\%$

Segment No.	q, exp MW/m^2	Segment No.	q, exp MW/m^2
1	0.6	13	30.3
2	1.3	14	45.5
3	1.7	15	47.8
4	2.6	16	25.4
5	3.4	17	21.7
6	4.4	18	14.7
7	5.9	19	7.7
8	6.8	20	5.9
9	7.9	21	4.5
10	10.8	22	3.8
11	15.4	23	2.3
12	23.3		

RUN 33

Pc = 6.92 MPa, O/F = 3.26, Mt = 1.72 kg/s, Tf = 274 K, $\eta c^* = 89.4\%$

Segment No.	q, exp MW/m^2	Segment No.	q, exp MW/m^2
1	0.6	13	34.2
2	1.4	14	52.4
3	1.6	15	51.5
4	2.4	16	27.4
5	3.1	17	22.8
6	4.1	18	17.4
7	5.9	19	8.8
8	7.0	20	5.6
9	8.2	21	5.0
10	11.7	22	4.4
11	16.8	23	2.8
12	25.5		

RUN 34

Pc = 5.23 MPa, O/F = 3.03, Mt = 1.28 kg/s, Tf = 269 K, $\eta c^* = 89.9\%$

Segment No.	q, exp MW/m^2	Segment No.	q, exp MW/m^2
1	0.7	13	29.0
2	1.4	14	39.3
3	1.6	15	44.2
4	2.4	16	20.9
5	3.1	17	20.5
6	4.1	18	14.1
7	5.7	19	6.6
8	6.4	20	4.1
9	7.2	21	3.9
10	9.2	22	3.3
11	13.9	23	2.1
12	20.8		

RUN 36

Pc = 7.11 MPa, O/F = 3.13, Mt = 1.66 kg/s, Tf = 775 K, $\eta c^* = 95.6\%$

Segment No.	q, exp MW/m^2	Segment No.	q, exp MW/m^2
1	11.9	13	36.0
2	11.3	14	54.4
3	10.4	15	50.4
4	11.2	16	31.5
5	11.1	17	23.8
6	11.2	18	15.7
7	11.6	19	9.6
8	12.3	20	7.4
9	13.2	21	4.9
10	16.7	22	4.1
11	20.5	23	2.6
12	26.5		

RUN 37

Pc = 7.08 MPa, O/F = 3.28, Mt = 1.64 kg/s, Tf = 794 K, $\eta c^* = 97.1\%$

Segment No.	q, exp MW/m^2	Segment No.	q, exp MW/m^2
1	12.3	13	38.5
2	11.5	14	56.7
3	10.8	15	55.2
4	11.5	16	31.9
5	11.6	17	25.1
6	11.7	18	16.7
7	12.2	19	9.8
8	12.7	20	7.9
9	13.9	21	5.2
10	17.7	22	4.3
11	21.8	23	2.7
12	29.2		

RUN 38

Pc = 7.07 MPa, O/F = 3.33, Mt = 1.64 kg/s, Tf = 724 K, $\eta c^* = 96.7\%$

Segment No.	q, exp MW/m^2	Segment No.	q, exp MW/m^2
1	11.6	13	40.8
2	10.3	14	48.0
3	10.0	15	50.1
4	11.1	16	35.2
5	11.3	17	26.3
6	11.6	18	17.6
7	11.9	19	10.9
8	12.8	20	8.2
9	13.7	21	5.6
10	17.8	22	4.7
11	22.6	23	3.0
12	30.8		

RUN 39

Pc = 6.97 MPa, O/F = 3.48, Mt = 1.60 kg/s, Tf = 868 K, $\eta c^* = 98.9\%$

Segment No.	q, exp MW/m^2	Segment No.	q, exp MW/m^2
1	13.6	13	41.4
2	15.5	14	57.7
3	12.0	15	55.9
4	12.6	16	35.8
5	12.4	17	27.3
6	12.5	18	18.8
7	12.9	19	10.7
8	13.6	20	8.5
9	15.0	21	5.7
10	19.1	22	4.7
11	24.4	23	3.1
12	32.8		

RUN 42

Pc = 8.18 MPa, O/F = 3.21, Mt = 1.94 kg/s, Tf = 911 K, $\eta c^* = 94.0\%$

Segment No.	q, exp MW/m^2	Segment No.	q, exp MW/m^2
1	11.9	13	38.4
2	12.4	14	54.4
3	11.4	15	47.5
4	11.8	16	30.8
5	11.8	17	24.4
6	11.7	18	17.3
7	12.2	19	10.6
8	12.7	20	8.5
9	13.7	21	5.7
10	17.2	22	4.8
11	20.9	23	3.1
12	28.4		

RUN 43

Pc = 9.61 MPa, O/F = 3.39, Mt = 2.27 kg/s, Tf = 860 K, $\eta c^* = 94.6\%$

Segment No.	q, exp MW/m^2	Segment No.	q, exp MW/m^2
1	10.3	13	48.8
2	11.2	14	70.4
3	10.8	15	59.0
4	12.3	16	37.8
5	12.7	17	30.3
6	13.1	18	21.2
7	14.0	19	12.8
8	14.8	20	10.3
9	16.2	21	6.9
10	20.5	22	5.5
11	25.2	23	3.2
12	34.6		

RUN 44

Pc = 8.80 MPa, O/F = 3.33, Mt = 2.08 kg/s, Tf = 800 K, $\eta c^* = 94.5\%$

Segment No.	q, exp MW/m²	Segment No.	q, exp MW/m²
1	9.3	13	49.1
2	10.1	14	70.4
3	9.9	15	62.1
4	11.4	16	37.9
5	11.8	17	29.8
6	12.2	18	20.5
7	13.1	19	12.2
8	13.9	20	9.8
9	15.5	21	6.6
10	19.5	22	5.3
11	24.7	23	3.5
12	33.5		

RUN 45

Pc = 9.03 MPa, O/F = 3.59, Mt = 2.14 kg/s, Tf = 818 K, $\eta c^* = 95.4\%$

Segment No.	q, exp MW/m²	Segment No.	q, exp MW/m²
1	9.7	13	49.7
2	10.6	14	71.4
3	10.3	15	59.5
4	11.8	16	37.9
5	12.3	17	30.4
6	12.7	18	21.2
7	13.6	19	12.7
8	14.6	20	10.3
9	16.1	21	6.9
10	20.3	22	5.6
11	25.3	23	3.7
12	34.1		

RUN 47

Pc = 8.97 MPa, O/F = 3.58, Mt = 2.12 kg/s, Tf = 786 K, $\eta c^* = 93.9\%$

Segment No.	q, exp MW/m²	Segment No.	q, exp MW/m²
CVT	10.2	14	20.8
1	10.7	15	24.3
2	10.9	16	33.4
3	11.1	17	43.7
4	11.5	18	60.5
5	11.7	19	58.5
6	11.8	20	39.3
7	11.9	21	30.9
8	11.9	22	20.4
9	12.6	23	12.8
10	12.2	24	–
11	13.2	25	–
12	14.4	26	–
13	16.4	27	–

RUN 48

Pc = 8.52 MPa, O/F = 4.67, Mt = 2.11 kg/s, Tf = 989 K, $\eta c^* = 95.0\%$

Segment No.	q, exp MW/m²	Segment No.	q, exp MW/m²
CVT	12.1	14	25.1
1	13.4	15	30.3
2	12.8	16	41.1
3	13.2	17	57.0
4	12.7	18	77.1
5	13.1	19	67.4
6	13.3	20	41.3
7	12.8	21	31.1
8	12.9	22	20.0
9	13.5	23	13.0
10	13.1	24	–
11	15.2	25	–
12	16.8	26	–
13	19.7	27	–

RUN 49

Pc = 7.15 MPa, O/F = 3.60, Mt = 1.69 kg/s, Tf = 769 K, $\eta c^* = 94.1\%$

Segment No.	q, exp MW/m²	Segment No.	q, exp MW/m²
CVT	10.1	14	21.0
1	9.9	15	25.2
2	10.0	16	35.3
3	10.4	17	48.7
4	10.2	18	65.4
5	10.8	19	56.5
6	10.8	20	35.2
7	10.6	21	26.1
8	10.9	22	17.3
9	11.3	23	11.3
10	10.9	24	–
11	12.7	25	–
12	14.0	26	–
13	16.4	27	–

RUN 50

Pc = 9.09 MPa, O/F = 3.35, Mt = 2.13 kg/s, Tf = 773 K, $\eta c^* = 94.1\%$

Segment No.	q, exp MW/m^2	Segment No.	q, exp MW/m^2
CVT	9.9	14	25.8
1	10.7	15	31.0
2	11.1	16	39.5
3	11.9	17	56.8
4	11.9	18	77.1
5	13.1	19	69.3
6	12.9	20	41.3
7	12.6	21	32.6
8	12.8	22	21.2
9	13.7	23	13.1
10	13.3	24	–
11	15.8	25	–
12	17.5	26	–
13	20.1	27	–

(3) LOX/RJ-1J Test Results

(a) FOOF Elements Injector

RUN 4

Pc = 5.28 MPa, O/F = 2.30, Mt = 1.28 kg/s, Tf = 280 K, $\eta c^* = 94.6\%$

Segment No.	q, exp MW/m^2	Segment No.	q, exp MW/m^2
1	1.5	13	27.1
2	2.2	14	39.9
3	2.2	15	28.5
4	2.6	16	14.1
5	3.2	17	10.7
6	3.6	18	7.2
7	4.4	19	4.4
8	5.4	20	3.5
9	6.5	21	2.6
10	8.7	22	2.5
11	11.9	23	1.8
12	18.0		

RUN 5

Pc = 7.37 MPa, O/F = 2.15, Mt = 1.77 kg/s, Tf = 281 K, $\eta c^* = 95.2\%$

Segment No.	q, exp MW/m^2	Segment No.	q, exp MW/m^2
1	1.7	13	40.3
2	2.9	14	53.1
3	3.2	15	35.3
4	3.8	16	17.0
5	4.6	17	13.2
6	5.3	18	9.1
7	6.4	19	5.1
8	7.7	20	4.1
9	9.1	21	3.0
10	12.3	22	2.5
11	17.4	23	1.7
12	27.0		

RUN 6

Pc = 8.59 MPa, O/F = 1.76, Mt = 2.03 kg/s, Tf = 280 K, ηc^* = 100.4%

Segment No.	q, exp MW/m²	Segment No.	q, exp MW/m²
1	10.8	13	46.5
2	11.8	14	60.7
3	10.9	15	42.2
4	10.8	16	21.9
5	10.5	17	15.4
6	10.4	18	9.4
7	11.8	19	4.8
8	13.0	20	3.7
9	15.0	21	3.2
10	19.6	22	2.7
11	25.9	23	1.8
12	35.4		

(b) FOF Element Injector

RUN 10

Pc = 5.07 MPa, O/F = 3.00, Mt = 1.24 kg/s, Tf = 273 K, ηc^* = 96.4%

Segment No.	q, exp MW/m²	Segment No.	q, exp MW/m²
1	1.5	13	25.3
2	1.7	14	39.4
3	2.1	15	29.3
4	2.9	16	15.8
5	3.4	17	12.3
6	3.9	18	8.7
7	4.9	19	5.2
8	5.6	20	4.0
9	6.4	21	2.9
10	8.3	22	2.5
11	11.1	23	1.7
12	16.6		

RUN 11

Pc = 7.18 MPa, O/F = 2.31, Mt = 1.71 kg/s, Tf = 280 K, ηc^* = 95.8%

Segment No.	q, exp MW/m²	Segment No.	q, exp MW/m²
1	2.1	13	24.9
2	2.8	14	43.0
3	3.7	15	30.1
4	4.0	16	16.9
5	4.6	17	11.5
6	4.5	18	7.8
7	5.9	19	4.6
8	5.7	20	3.6
9	7.1	21	2.8
10	8.7	22	2.7
11	11.9	23	1.7
12	16.9		

RUN 12

Pc = 7.21 MPa, O/F = 2.46, Mt = 1.72 kg/s, Tf = 275 K, ηc^* = 96.3%

Segment No.	q, exp MW/m²	Segment No.	q, exp MW/m²
1	2.9	13	32.2
2	3.3	14	47.0
3	3.9	15	33.9
4	4.7	16	17.2
5	4.8	17	13.2
6	5.4	18	8.9
7	6.3	19	5.3
8	6.9	20	4.0
9	7.8	21	2.8
10	10.1	22	2.6
11	13.5	23	1.7
12	20.2		

RUN 14

Pc = 10.4 MPa, O/F = 2.36, Mt = 2.44 kg/s, Tf = 278 K, ηc^* = 97.0%

Segment No.	q, exp MW/m²	Segment No.	q, exp MW/m²
1	2.5	13	49.5
2	4.0	14	75.0
3	5.8	15	55.2
4	6.9	16	31.4
5	8.5	17	22.9
6	8.1	18	14.5
7	10.6	19	7.5
8	10.5	20	5.9
9	13.7	21	3.7
10	18.3	22	3.2
11	25.7	23	2.0
12	38.4		

RUN 15

Pc = 10.43 MPa, O/F = 2.44, Mt = 2.44 kg/s, Tf = 277 K, ηc^* = 97.3%

Segment No.	q, exp MW/m²	Segment No.	q, exp MW/m²
1	3.6	13	46.2
2	4.7	14	60.3
3	5.8	15	54.5
4	7.4	16	28.9
5	8.1	17	21.7
6	8.9	18	14.5
7	10.6	19	8.4
8	12.2	20	6.5
9	14.7	21	4.3
10	20.5	22	3.9
11	27.9	23	2.3
12	37.4		

RUN 45

Pc = 10.08 MPa, O/F = 3.36, Mt = 2.46 kg/s, Tf = 299 K, ηc^* = 98.9%

Segment No.	q, exp MW/m^2	Segment No.	q, exp MW/m^2
CVT	1.7	14	25.1
1	2.1	15	32.4
2	3.5	16	44.7
3	4.2	17	61.6
4	6.7	18	88.0
5	9.8	19	89.1
6	10.5	20	–
7	11.7	21	44.6
8	12.2	22	26.4
9	13.2	23	15.2
10	13.3	24	–
11	14.7	25	–
12	16.6	26	–
13	19.0	27	–

RUN 46

Pc = 10.21 MPa, O/F = 2.47, Mt = 2.42 kg/s, Tf = 299 K, ηc^* = 97.4%

Segment No.	q, exp MW/m^2	Segment No.	q, exp MW/m^2
CVT	2.8	14	17.5
1	3.2	15	21.5
2	3.6	16	34.5
3	2.8	17	54.1
4	5.5	18	74.6
5	7.8	19	70.4
6	7.6	20	39.6
7	8.7	21	26.9
8	8.9	22	14.8
9	9.6	23	8.2
10	9.7	24	–
11	10.7	25	–
12	11.5	26	–
13	13.1	27	–

RUN 47

Pc = 10.19 MPa, O/F = 2.55, Mt = 2.41 kg/s, Tf = 300 K, ηc^* = 97.7%

Segment No.	q, exp MW/m^2	Segment No.	q, exp MW/m^2
CVT	2.5	14	18.5
1	3.2	15	24.6
2	3.7	16	28.3
3	3.4	17	54.3
4	5.8	18	76.9
5	8.0	19	72.8
6	8.0	20	41.0
7	9.2	21	28.6
8	9.2	22	15.6
9	10.0	23	8.4
10	10.1	24	–
11	11.1	25	–
12	12.3	26	–
13	13.9	27	–

RUN 48

Pc = 10.27 MPa, O/F = 2.83, Mt = 2.45 kg/s, Tf = 300 K, ηc^* = 98.1%

Segment No.	q, exp MW/m^2	Segment No.	q, exp MW/m^2
CVT	2.0	14	25.0
1	2.6	15	33.1
2	3.6	16	33.3
3	4.1	17	61.7
4	6.3	18	82.9
5	8.9	19	80.5
6	9.8	20	52.4
7	10.3	21	35.7
8	10.6	22	22.7
9	11.7	23	14.9
10	11.6	24	–
11	13.0	25	–
12	14.6	26	–
13	16.5	27	–

RUN 49

Pc = 10.24 MPa, O/F = 3.08, Mt = 2.47 kg/s, Tf = 303 K, $\eta c^* = 98.6\%$

Segment No.	q, exp MW/m^2	Segment No.	q, exp MW/m^2
CVT	1.9	14	25.0
1	2.8	15	33.1
2	4.0	16	33.3
3	4.9	17	61.7
4	7.1	18	82.9
5	10.0	19	80.5
6	11.0	20	52.4
7	11.6	21	35.7
8	11.8	22	22.7
9	13.3	23	14.9
10	13.2	24	–
11	13.2	25	–
12	15.0	26	–
13	18.9	27	–

RUN 50

Pc = 10.17 MPa, O/F = 2.26, Mt = 2.42 kg/s, Tf = 303 K, $\eta c^* = 96.9\%$

Segment No.	q, exp MW/m^2	Segment No.	q, exp MW/m^2
CVT	2.6	14	15.7
1	3.8	15	20.2
2	4.2	16	19.1
3	3.6	17	49.0
4	5.0	18	65.9
5	7.0	19	58.7
6	7.0	20	24.4
7	7.8	21	21.5
8	7.7	22	11.1
9	8.6	23	7.3
10	8.5	24	–
11	9.3	25	–
12	10.3	26	–
13	11.8	27	–

RUN 51

Pc = 10.31 MPa, O/F = 2.62, Mt = 2.47 kg/s, Tf = 301 K, $\eta c^* = 96.8\%$

Segment No.	q, exp MW/m^2	Segment No.	q, exp MW/m^2
1	1.9	15	23.9
2	1.7	16	36.7
3	1.0	17	53.0
4	2.4	18	71.9
5	4.2	19	68.0
6	4.6	20	40.1
7	6.0	21	27.9
8	6.5	22	14.3
9	8.2	23	8.8
10	8.4	24	5.6
11	9.7	25	–
12	11.2	26	–
13	12.9	27	–
14	17.3		

RUN 52

Pc = 10.24 MPa, O/F = 2.68, Mt = 2.45 kg/s, Tf = 300 K, $\eta c^* = 97.1\%$

Segment No.	q, exp MW/m^2	Segment No.	q, exp MW/m^2
1	2.1	15	24.7
2	2.3	16	38.5
3	0.9	17	55.5
4	3.3	18	73.4
5	5.7	19	71.1
6	6.1	20	42.1
7	7.5	21	28.2
8	7.8	22	15.2
9	9.2	23	9.2
10	9.4	24	5.8
11	10.6	25	–
12	12.2	26	–
13	13.8	27	–
14	18.5		

RUN 53

Pc = 10.38 MPa, O/F = 2.34, Mt = 2.48 kg/s, Tf = 299 K, ηc^* = 96.1%

Segment No.	q, exp MW/m^2	Segment No.	q, exp MW/m^2
1	1.9	15	18.3
2	1.9	16	29.6
3	0.5	17	48.2
4	1.7	18	64.3
5	2.8	19	61.3
6	2.7	20	38.7
7	3.6	21	20.6
8	3.9	22	12.0
9	5.1	23	7.2
10	5.7	24	4.6
11	7.0	25	–
12	8.2	26	–
13	9.6	27	–
14	12.7		

RUN 54

Pc = 10.27 MPa, O/F = 2.69, Mt = 2.45 kg/s, Tf = 298 K, ηc^* = 97.6%

Segment No.	q, exp MW/m^2	Segment No.	q, exp MW/m^2
1	2.7	15	27.1
2	3.3	16	42.1
3	4.9	17	62.5
4	4.7	18	87.6
5	7.4	19	86.1
6	8.0	20	43.4
7	8.9	21	33.4
8	9.1	22	18.8
9	10.4	23	10.5
10	10.4	24	6.9
11	11.8	25	–
12	13.4	26	–
13	15.3	27	–
14	20.3		

RUN 55

Pc = 10.27 MPa, O/F = 2.82, Mt = 2.46 kg/s, Tf = 298 K, ηc^* = 97.6%

Segment No.	q, exp MW/m^2	Segment No.	q, exp MW/m^2
1	2.3	15	27.1
2	3.1	16	40.8
3	4.8	17	57.1
4	5.0	18	73.6
5	7.8	19	72.2
6	8.6	20	44.7
7	9.6	21	30.9
8	9.7	22	17.2
9	11.1	23	10.3
10	11.1	24	6.6
11	12.4	25	–
12	13.7	26	–
13	15.6	27	–
14	20.3		

TECHNICAL REPORT OF NATIONAL
AEROSPACE LABORATORY
TR-1062T

航空宇宙技術研究所報告1062T号（欧文）

平成2年4月発行

発行所　航空宇宙技術研究所
東京都調布市深大寺東町7丁目44番地1
電話武蔵野三鷹(0422)47-5911(大代表)〒182
印刷所　株式会社　東京プレス
東京都板橋区桜川2－27－12

Published by
NATIONAL AEROSPACE LABORATORY
7-44-1 Jindaijihigashi-Machi Chōfu, Tokyo
JAPAN

Printed in Japan